Convective and Turbulent Motions in Nonprecipitating Cu. Part II: LES Simulated Cloud Represented by a Starting Plume

MARK PINSKY,[a] ESHKOL EYTAN,[b] ILAN KOREN,[b] AND ALEXANDER KHAIN[a]

[a] Department of Atmospheric Sciences, Hebrew University of Jerusalem, Jerusalem, Israel
[b] Department of Earth and Planetary Science, Weizmann Institute of Science, Rehovot, Israel

(Manuscript received 25 May 2021, in final form 5 December 2021)

ABSTRACT: The dynamic structure of a small trade wind cumulus (Cu) is analyzed using a novel approach. Cu developing in a shear-free environment is simulated by 10-m-resolution LES model with spectral bin microphysics. The aim is to clarify the dynamical nature of cloud updraft zone (CUZ) including entrainment and mixing in growing Cu. The validity of concept stating that a cloud at developing state can be represented by a parcel or a jet is tested. To investigate dynamical entrainment in CUZ performed by motions with scales larger than the turbulence scales, the modeled fields of air velocity were filtered by wavelet filter that separated convective motions from turbulent ones. Two types of objects in developing cloud were investigated: small volume ascending at maximal velocity (point parcel) and CUZ. It was found that the point parcel representing the upper part of cloud core is adiabatic. The motion of the air in this parcel ascending from cloud base determines cloud-top height. The top-hat (i.e., averaged) values of updraft velocity and adiabatic fraction in CUZ are substantially lower than those in the point parcel. Evaluation of the terms in the dynamical equation typically used in 1D cloud parcel models show that this equation can be applied for calculation of vertical velocities at the developing stage of small Cu, at least up to the heights of the inversion layer. Dynamically, the CUZ of developing cloud resembles the starting plume with the tail of nonstationary jet. Both the top-hat vertical velocity and buoyancy acceleration linearly increase with the height, at least up to the inversion layer. An important finding is that lateral entrainment of convective (nonturbulent) nature has a little effect on the top-hat CUZ velocity and cannot explain the vertical changes of conservative variables q_t and θ_l. In contrast, entrained air lifting inside CUZ substantially decreases top-hat liquid water content and its adiabatic fraction. Possible reasons of these effects are discussed.

SIGNIFICANCE STATEMENT: (i) The study improves the understanding of the effects of lateral entrainment and mixing. (ii) The study shows the dominating role of the convective-scale motions in cloud microphysics and dynamics. (iii) The comparison of results of 10-m-resolution large-eddy simulations with a simple cloud model allows evaluating validity of current schemes of convective parameterization.

KEYWORDS: Cumulus clouds; Mixing; Convective parameterization; Large eddy simulations

1. Introduction

The main component of many mass flux convective parameterizations in large-scale atmospheric and climate models is the cloud parcel model or jet model (Arakawa and Schubert 1974; Tiedtke 1989; Plant and Yano 2015). In these models, convective clouds can be represented in three ways: 1) as a steady turbulent jet entraining the surrounding air through lateral sides, 2) as a pop-up bubble (thermal), which traces the ascending element of buoyant fluid, and 3) as a "starting plume," which is combination of the first two configurations.

The representation of a convective cloud as a steady state convective plume (jet) was supposedly first introduced by Stommel (1947), while Scorer and Ludlam (1953) proposed representing cumulus (Cu) by a succession of buoyant bubbles. Since interaction of bubbles with entrainment air differs significantly from that of plumes, Romps et al. (2015) analyzed a large amount of small Cu to determine whether the Cu resemble bubbles or plumes, using observed data and LES. The ratio of mass within cloud and the mass flux was chosen as a criterion for such separation.

The starting plume (Turner 1962) represents a nonstationary jet capped by an ascending head bubble. According to McCarthy (1974), starting plumes representation describes the evolution of Cu better than stationary jets or bubbles. Multiple studies have been dedicated to analysis of the structure of convective clouds, both small Cu and deep convective ones (e.g., Blyth et al. 1988, 2005, and references therein). The results of in situ measurements were compared with the results of laboratory experiments mimicking cloud development.

It was found in laboratory experiments that the internal circulation in a rising bubble resembles a toroidal vortex (a coherent vortical circulation) (Blyth et al. 1988, 2005; Zhao and Austin 2005; Shusser and Gharib 2000; Pruppacher and Klett 1997, Fig. 12.3) with updraft in the bubble center, divergence at the top and downdraft at periphery. Sometimes, cloud may consist of a few bubbles with the same properties, namely, updrafts in the center and downdrafts at the periphery.

An important problem related to cloud dynamics and microphysics is that of cloud interaction with its environment. It is accepted to describe such interaction in terms of

Corresponding author: Alexander Khain, alexander.khain@mail.huji.ac.il

DOI: 10.1175/JAS-D-21-0137.1

entrainment/detrainment and mixing. According to several studies, entrainment into clouds takes place via lateral cloud boundaries, and the effects of mixing are observed at the horizontal levels close to those of the penetration level (Heus and Jonker 2008; de Rooy et al. 2013).

Analysis of small parametric 1D cloud parcel models widely used for convective parameterization is useful for investigation of entrainment because the dynamic, thermodynamic, and microphysical parts of the models describe the entrainment in the simplest way. Actually, parcel models mimic the air ascending zone of convective clouds (typically at developing stage).

The typical equation system describing a horizontally uniform rising bubble or vertical jet can be found in Pruppacher and Klett (1997). The changes of vertical velocity W of the ascending bubble or the velocity in a jet are described by an equation

$$\frac{dW}{dt} = W\frac{dW}{dz} = \frac{1}{1+\gamma}B - \frac{E}{1+\gamma}W^2, \tag{1}$$

where B is the buoyancy force (per unit of mass), E is entrainment rate, and $\gamma = 0.5$ is the virtual mass coefficient that describes the effect of decrease of "induced mass" and pressure effects. The first term on the right-hand side of Eq. (1) reflects the buoyancy force, and the second term is friction-like term, which decreases W via entrainment of unmovable environment air. The buoyancy is calculated as

$$B \approx g\left\{\frac{T - T_0}{T_0} + 0.61(q_v - q_{v0}) - q_l\right\}, \tag{2}$$

where g is gravity acceleration, T is absolute temperature in the parcel, q_v is water vapor mixing ratio, and q_l is liquid water mixing ratio. The remaining terms, T_0 and q_{v0}, are reference values measured far from the cloud. The entrainment rate in the model is calculated as the ratio

$$E = \frac{2\alpha}{R} = \frac{0.2}{R} \quad \text{for jet} \tag{3a}$$

or

$$E = \frac{3\alpha}{R} = \frac{0.6}{R} \quad \text{for bubble,} \tag{3b}$$

where α is the entrainment coefficient (Levine 1959; Simpson and Wiggert 1969) and R is the radius of the equivalent jet or bubble.

Uncertainties of the 1D parcel models, related to the geometric parameters, cloud-top height, and other factors, lead to the fact that different studies use different values of the Eq. (1) coefficients in the modern versions of parcel models [see de Roode et al. (2012) and references in this study]. So a more general equation is often used instead of Eq. (1):

$$W\frac{dW}{dz} = c_1 B(z) - c_2(z)W^2, \tag{4}$$

where c_1 and c_2 are coefficients. Equations (1) and (4) are often formulated on the basis of convective nature of entrainment (hereafter the entrainment performed by motions with scales larger than the turbulence scales will be referred to as dynamic entrainment). The "convective" interpretation of Eq. (4) is very important, since convective-scale motion may be the main source of both vertical mass and energy fluxes through the lateral boundary of the cloud, at least at the developing stage of cloud evolution.

In addition to dynamic equations, Eqs. (1) or (4), the parcel models are also used to calculate thermodynamic variables that are also assumed uniform within the bubble (or in the horizontal cross section of vertical jet). To evaluate the effect of lateral entrainment on thermodynamic variables, we use the simplest equations used in parcel models for variables that are conservative in moist adiabatic processes. These variables are the total water mixing ratio q_t and liquid water potential temperature θ_l, determined as

$$q_t = q_v + q_l, \tag{5}$$

$$\theta_l = (T + \gamma_a z)\left(1 - \frac{L_w q_l}{c_p T}\right), \tag{6}$$

where q_v is water vapor mixing ration, and $\gamma_a = 9.8 \times 10^{-3}\,°\mathrm{C\,m^{-1}}$ is the dry adiabatic gradient (see Pruppacher and Klett 1997; Khain and Pinsky 2018). Other variables are presented in appendix C. The thermodynamic equations for these variables are (Pruppacher and Klett 1997)

$$\frac{dq_t}{dz} = -E(q_t - \tilde{q}_t) + Q_t, \tag{7}$$

$$\frac{d\theta_l}{dz} = -E(\theta_l - \tilde{\theta}_l) + Q_l, \tag{8}$$

where $\tilde{q}_t(z)$ and $\tilde{\theta}_l(z)$ are the values of total water mixing ratio and liquid water potential temperature outside the cloud, respectively. In Eqs. (7) and (8) the first terms on the right-hand sides describe the influence of entrained air, while the last terms characterize other mechanisms that may affect q_t and θ_l.

Equations (1)–(8) are written for dynamical and thermodynamic quantities averaged over a bubble, or over the horizontal cross section of a jet. In such approach, the bubble is characterized by a single vertical velocity and a certain temperature. If a cloud is identified with this bubble, the entrainment changes cloud properties immediately within the entire cloud. In reality, the process of entrainment and mixing is much more complicated, resulting in inhomogeneity of the cloud. Nevertheless, it is quite convenient to use these equations to evaluate effects of entrainment on cloud dynamics and microphysics. This analysis would be useful if cloud models reasonably represented properties of real clouds.

Several studies investigated processes of entrainment using either observations or large-eddy simulations (LES) and direct numerical simulations (DNS) (Norgren et al. 2016; de Rooy and Siebesma 2010; Abma et al. 2013; Nair et al. 2020). For instance, de Roode et al. (2012) evaluated the terms in the dynamical Eq. (4) using LES of an ensemble of small Cu observed during ARM and BOMEX experiments. In particular, it was found that the entrainment term [the second term on the right-hand side of Eq. (4)] is substantially smaller than the first term. According to de Roode et al. (2012), the decrease in W takes place due to the decrease in "effective" buoyancy. The latter is attributed to the effect of pressure fluctuations, which cause decrease in the coefficient c_1 in the Eq. (4) or increase in coefficient γ in the Eq. (1). The entrainment term in that study was not calculated directly, but was found as residual.

In the present study, we investigate dynamic, thermodynamic, and microphysical properties of cloud updraft zone (CUZ), which is coherent (nonrandom) structure of the updraft. We try to clarify the role of the lateral dynamic entrainment in the vertical changes of W, q_t, θ_l, and liquid water content (LWC) in comparison with other mechanisms that should be taken into account. We also try to evaluate the extent to which Cu can be represented by a 1D parcel model and, in particular, what representation—a bubble or a jet—describes cloud properties better. This question is closely related to the problem of validity of mass-flux convection parameterizations. To answer both questions, we simulate a single Cu typical of trade wind zone (BOMEX) using 10-m high-resolution LES model with spectral bin microphysics and analyze the simulated results using wavelet filtering (Pinsky et al. 2021). This novel approach makes it possible to distinguish convective and turbulent factors determining thermodynamic and microphysical structures of cloud.

2. Model and data processing

a. Model

In this study we use the System Atmospheric Modeling (SAM), a 3D LES model first formulated by Khairoutdinov and Kogan (2000) and Khairoutdinov and Randall (2003). SAM is designed to simulate fine thermodynamic and microphysical cloud structures at high resolution (10 m), which allows direct reproducing of both convective and turbulent motions. The specific feature of the SAM version is usage of spectral bin microphysics (Khain et al. 2004; Khain and Pinsky 2018). Generally, the scheme describes mixed-phase microphysics and calculates size distribution (SD) functions of water drops, of 3 types of ice crystals (planar, dendrites, and columns), aggregates (snow), as well as of graupel and hail. Particles of each mass and type are characterized by their density, shape, and fall velocity. All SDs are defined on logarithmically equidistant (mass doubling) mass grid containing 33 bins and completely covering all the possible sizes of raindrops up to 8 mm in diameter. To describe cloud droplet formation and cloud–aerosol interaction as a whole, a separate SD for aerosols is calculated. The rates of diffusion growth/evaporation are calculated by solving a system of equations for supersaturation, together with the equations for diffusion growth/evaporation of droplets. The changes in drop size distribution (DSD) resulting from collisions between drops, are calculated by solving the stochastic collision equations (Khain and Pinsky 2018). The height dependencies of collision efficiencies and collision kernels for drops are calculated offline.

SAM with spectral bin microphysics has been successfully used for simulation of different types of clouds (Fan et al. 2011; Ovchinnikov et al. 2014; Heiblum et al. 2016; Khain et al. 2019). In this study, we simulated a small trade wind warm nonprecipitating Cu at resolution of 10 m. The BOMEX-1974 sounding profiles (Fig. 1) are used in the course of simulations. One can see the presence of temperature inversion layer at the height of 1400–2000 m over the surface, in which temperature decreases by 0.25°C. The humidity and relative humidity rapidly decrease in the inversion layer. There is no mean wind shear in the cloud environment, so the single source of cloud convection is the vertical temperature gradient. In this way, we simulate the Cu with the simplest convection structure and well-defined CUZ inside the cloud. We defined CUZ as a cloud region of horizontal cross section $S(x, y)$, which obeys the conditions for convective updraft velocity $W(x, y) > 0.1$ m s^{-1}, and for the LWC $q(x, y) > 0.01$ g kg^{-1}. Besides, the cross-sectional area was chosen to be larger than 50×50 m^2 to eliminate small cloudy volumes in the surrounding of the main cloud. The constraint imposed on the cross-sectional area just influences the lower and upper boundaries of the analyzed height range. Supplemental calculations show that even such a sensitive parameter as top-hat adiabatic fraction inside CUZ changes by no more than 10% below the inversion level and by no more than 20%–25% inside of and above the inversion level, when restrictions $W(x, y) > 0.1$ m s^{-1} and $q(x, y) > 0.01$ g kg^{-1} change by a factor of 2.

b. Wavelet processing

Outside CUZ the air may descend forming subsiding shells. Besides, a cloud is spatially nonhomogeneous object in which zones of regular convective updraft and downdraft are superimposed by random turbulent motions. Due to these reasons, we applied 2D spatial wavelet filtering to separate convective and turbulent motions, as described in Part I of the study (Pinsky et al. 2021). The characteristic feature of the wavelet analysis is the ability to perform filtration in local areas of a long-lasting nonstationary signal. The mathematical theory of wavelets is presented by Daubechies (1992).

We represent the modeled field of the vertical velocity component at every output time step (0.5 min) as a set of horizontal slices $w_i(x, y)$ with a height increment of 10 m. Every slice is filtered using both low-frequency and high-frequency wavelet filters. Low-frequency signals correspond to convective velocity $W(x, y)$ to be used in our analysis, while high-frequency signals correspond to turbulent velocity $w'(x, y)$, which has approximately zero sum over the whole slice. Therefore, the total vertical velocity is represented (as assumed by the conventional definition of turbulence) as a sum

$$w(x, y) = W(x, y) + w'(x, y). \tag{9}$$

The horizontal components of air velocity are filtered analogously.

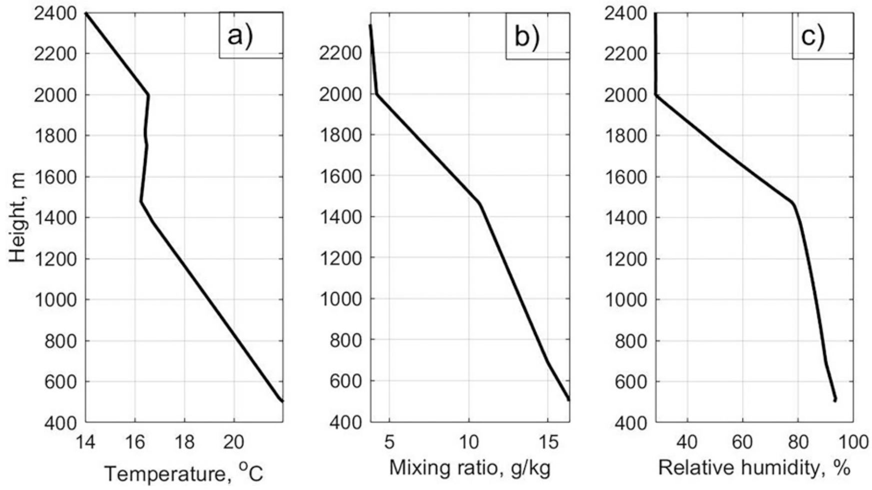

FIG. 1. Vertical profiles of (a) temperature, (b) the mixing ratio of water vapor, and (c) the relative humidity of the air, measured far from cloud.

It should be stressed that the retrieval of convective (systematic) field from the total motion filed cannot be performed by averaging the results of simulations using slightly perturbed initial conditions. The matter is that perturbations of the initial conditions lead to different convective fields, i.e., to different cloud shapes, due to nonlinearity of cloud processes. On the other hand, a specific feature of wavelet analysis is the ability to perform filtration in localized areas of a long-lasting nonstationary signal, which makes it possible to detect the CUZ that may have very sharp boundaries, so the locality of filtration is of great importance. Application of alternative methods such as temporal averaging window has a number of disadvantages. For example, it requests data output volume that is by two orders larger, imposing a serious limitation of 3D high-resolution cloud model.

Then, in order to isolate the CUZ, additional conditions mentioned in section 2a were imposed on analyzing $W(x, y)$ 2D fields. This technique makes it possible to confidently isolate CUZ and eliminate small isolated volumes arising away from the CUZ in the course of cloud development. An example of $W(x, y)$ slice obtained after wavelet filtering and contouring the core region, is shown in Fig. 2a. The corresponding initial velocity field $w(x, y)$ is shown in Fig. 2b for comparison. It is seen that wavelet filtering allows distinctly highlight large-scale convective velocity structure forming clouds skeleton. One can see that the center of the cloud is occupied by a CUZ with an upward convective flow. This CUZ is surrounded by a subsiding shell with characteristic width of 100–300 m. The initial nonfiltered vertical velocity field shown in Fig. 2b is asymmetric. The main reason for such

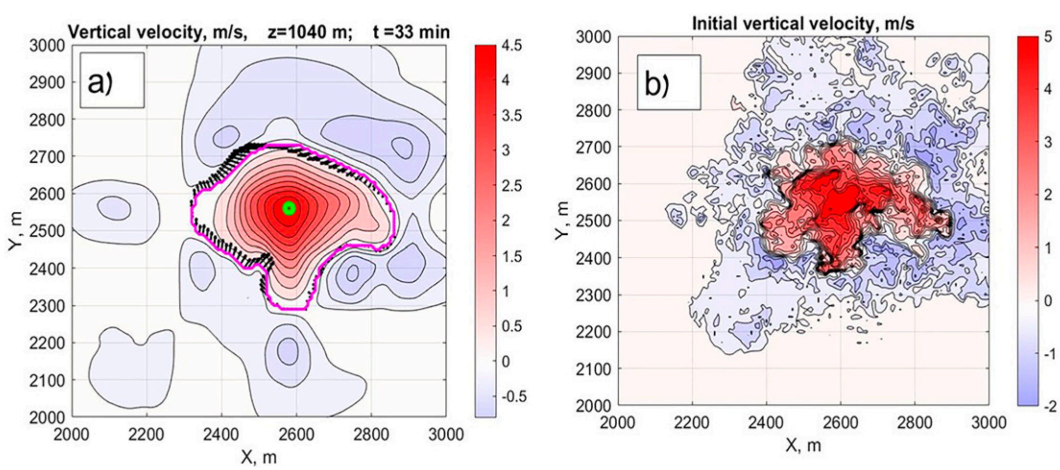

FIG. 2. (a) An example of a horizontal slice of the vertical velocity at convective scales filtered out by wavelet. The CUZ is clearly seen. The boundary of CUZ is shown by the magenta line. The vectors of the horizontal velocity at CUZ boundary are shown by arrows. The point of the maximum vertical velocity on the center of the CUZ is shown by green. (b) Horizontal slice of the vertical velocity before filtering.

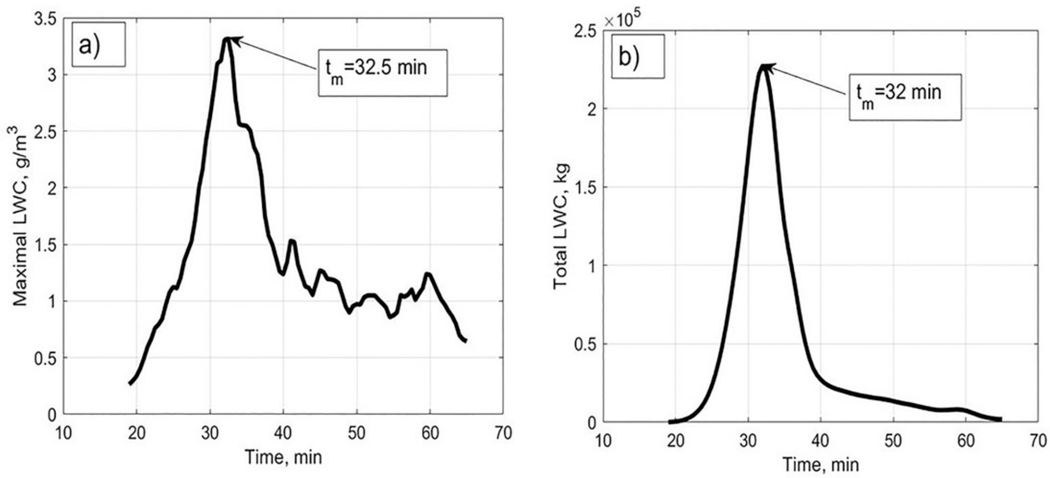

FIG. 3. (a) Time dependence of maximum LWC (g m^{-3}). (b) Time dependence of total LWC in the cloud (kg).

asymmetry is nonsymmetric initial conditions at cloud base. The wavelet filtering process is tuned to this asymmetry due to the locality of the filtration.

3. Three stages of cloud evolution

It is known that evolution of Cu clouds includes three stages (Katzwinkel et al. 2014). The first stage is the stage of active growth characterized by existing of rising cloud CUZ in which LWC increases with height. This stage is also characterized by positive buoyancy force. The second stage is deceleration when the cloud air continues to rise, but with a deceleration caused by negative buoyancy force. The third dissolving stage is characterized by negative buoyancy force that creates downdrafts leading to cloud dissipation.

The three development stages manifest themselves in temporary changes of the dynamic, microphysical, and geometric characteristics of a cloud. The most important microphysical characteristic of a warm cloud is LWC. Figure 3a demonstrates the time dependence of maximum LWC. At first, the maximum LWC increases till time instance of t_m = 32.5 min and then decreases. The maximum value of the maximal LWC is equal to ~3.3 g m^{-3}. The presence of a long tail of LWC of ~1 g m^{-3} and lasting from 43 to 63 min is clearly seen in the figure. The analogous tail on the time dependence of total cloud water content shown in Fig. 3b, is not so pronounced. Actually, after 40 min the cloud crumbled into several parts, including small volumes having, however, a significant LWC on the order of 1 g m^{-3}. These small volumes can be considered as new small clouds. From Fig. 3 one can conclude that the total lifetime of the modeled cloud is equal to ~43 min.

The geometrical parameters of the cloud also change during its evolution. The cloud-top height first increases reaching 2400 m at t_m = 33.5 min and then decreases (Fig. 4a). The CUZ width ranges between 200 and 600 m. (Fig. 8). The mean volume size of the cloud also changes with time,

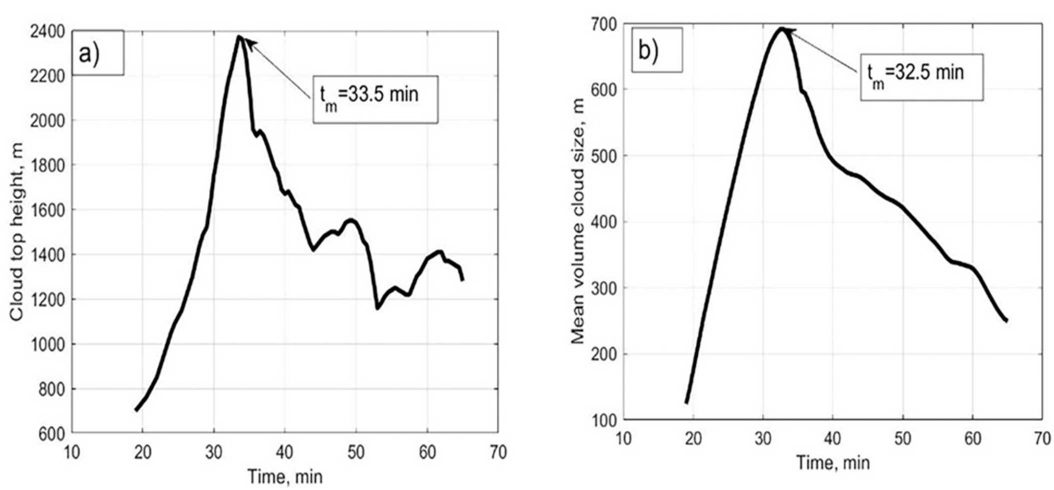

FIG. 4. (a) Time dependence of the cloud-top height. (b) Time dependence of the mean volume cloud size.

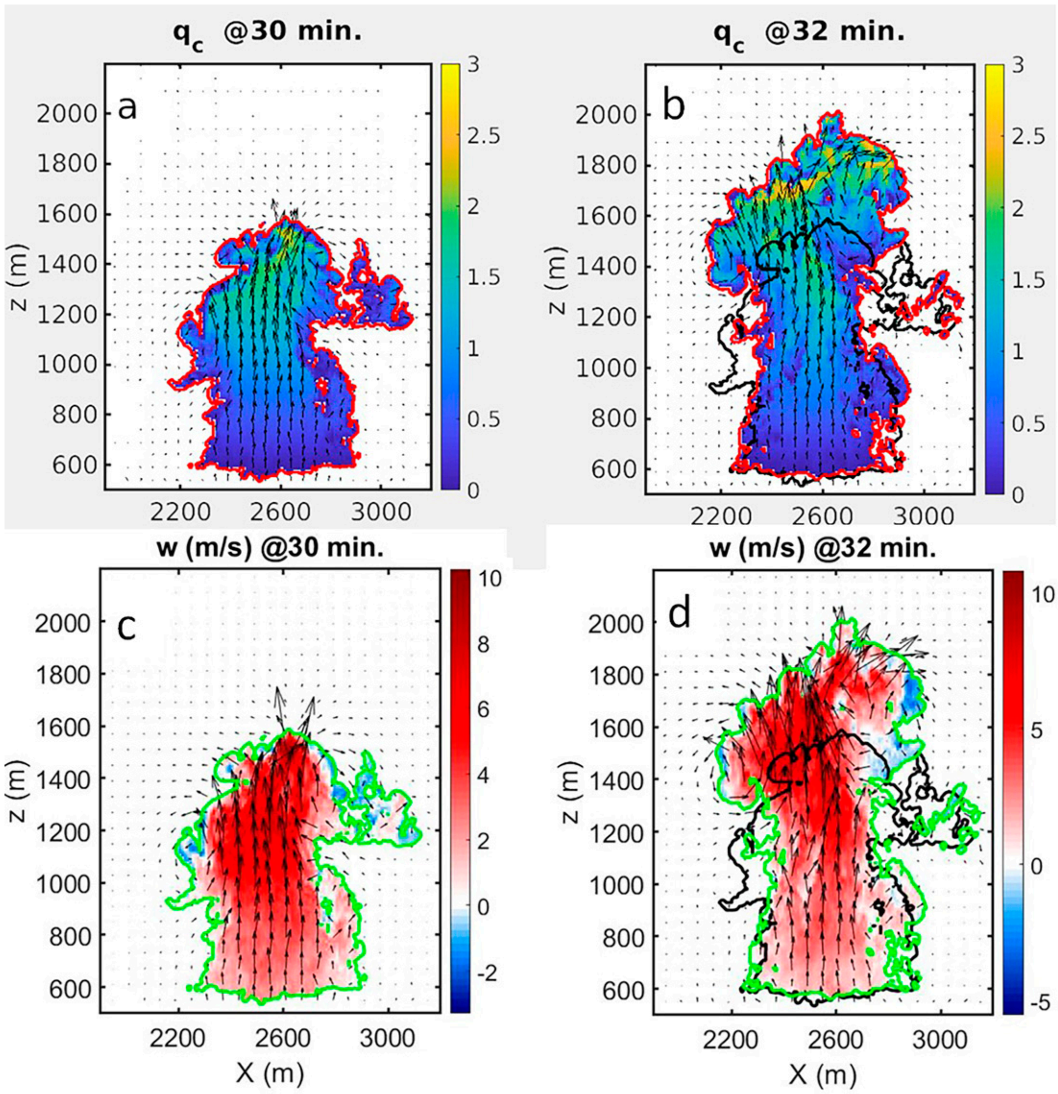

FIG. 5. Vertical cross sections of (a),(b) LWC and (c),(d) of w, at 30 and 32 min. Black lines in (b) and (d) mark the cloud boundary at 30 min. Arrows indicate the air velocities.

reaching the maximum value of about 700 m at $t_m = 32.5$ min (Fig. 4b). In general, the evolution of the cloud demonstrates well-pronounced asymmetry. Both LWC and geometrical characteristics demonstrate fast growth of Cu (~14 min) and then its slow dissipation (32 min), accompanied apparently by cloud splitting into several parts. Such cloud sizes and lifetimes are typical for nonprecipitating Cu (e.g., Gerber 2000; Gerber et al. 2008; Heus et al. 2009).

To better illustrate the simulated cloud at the developing and mature stages, we present Fig. 5 showing vertical cross sections of LWC and vertical velocity w at 30 and 32 min. One can see that both LWC and w increase with height, and are inhomogeneous in the horizontal direction. Analysis of the velocity field shows the existence of divergence near the cloud top and existence of downdrafts near the cloud edges. This structure can be interpreted as a toroidal vortex in the upper part of the cloud (see, e.g., Houze 2014, Fig. 7.9). Interestingly, the top of the cloud ascends vertically at approximately the same definite speed, remaining approximately parallel to its previous position, despite the different vertical velocities in the cloud core and at the periphery. This effect can be attributed to the vortex dynamics forming the divergence.

4. Point parcel model

Now we try to answer the question formulated in the introduction: "Can a nonprecipitating Cu at the development stage be represented by either an ascending bubble or a steady jet?" We start with the analysis of height–time changes of the maximum vertical velocity $W_{max}(z, t)$. The zone of the cloud with maximum vertical velocity will be referred to as the

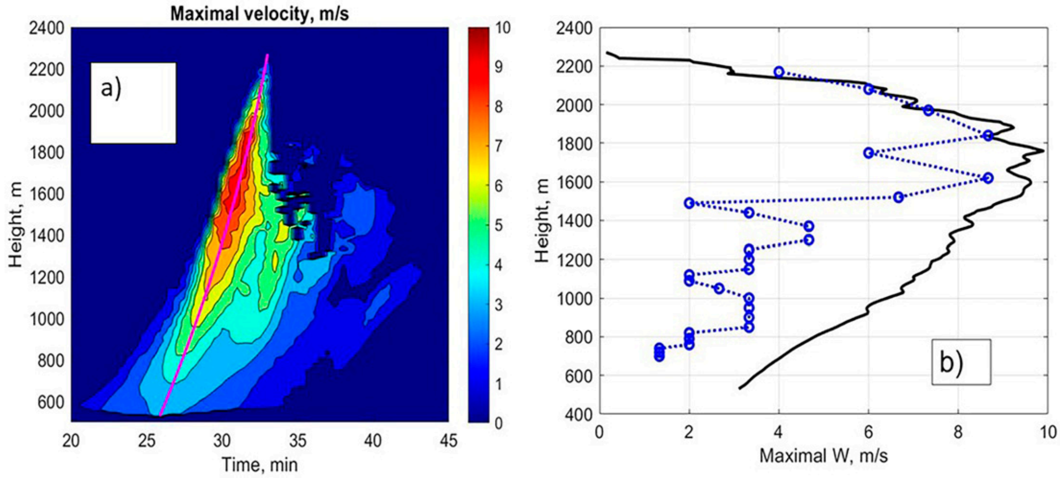

FIG. 6. (a) Height–time field of $W_{max}(z, t)$. The magenta line shows z–t trajectory of the rising point parcel. (b) Vertical profile of the velocity of the point parcel (black solid line) and the velocity of the cloud-top ascent (blue dotted line). The cloud-top height is defined as the maximum height where LWC exceeds 0.01 g kg^{-1}.

cloud core. The spatial coordinates of points corresponding to W_{max} lie inside the CUZ determined by boundary (example shown in Fig. 2). The height–time field of $W_{max}(z, t)$ is shown in Fig. 6a. One can see that the cloud core characterized by $W_{max}(z, t)$ does not behave like a stationary vertical jet [in this case, the contours of $W_{max}(z, t)$ would form long horizontal bands]. At the same time, Fig. 6a allows one to detect some kind of a rising object leaving a trail. Therefore, Fig. 6a is rather consistent with the concept of a starting plume, i.e., nonstationary jet capped by a rising head bubble whose z–t trajectory is shown by the magenta line in Fig. 6a. [This z–t trajectory is determined by $W_{max}(z, t)$ at each height and each time instances.] The vertical profile of the maximal velocity in this head bubble is shown in Fig. 6b. The velocity increases with height up to $z = 1800$ m and then decreases rapidly due to negative buoyancy. Interestingly, the velocity continues growing for some time in the inversion layer. Below the head bubble, there is a jet-like tail with W_{max} decreasing with time.

The velocity of the cloud-top ascent, also shown in Fig. 6b, is lower than the maximum air velocity in the head bubble. This is an evidence of the existence of mass divergence near the cloud top from the zone of maximum updraft, in agreement with the velocity field shown in Fig. 5. This divergence created mushroom-like clouds indicates the existence of a toroidal vortex near the cloud top (see, e.g., Houze 2014, Fig. 7.9).

Calculations of LWC at points of maximum updraft velocity show that the cloud core continues to be undiluted or slightly diluted for a long time, as seen in Fig. 7. Quasi-horizontal segments of isolines in Fig. 7a correspond to the

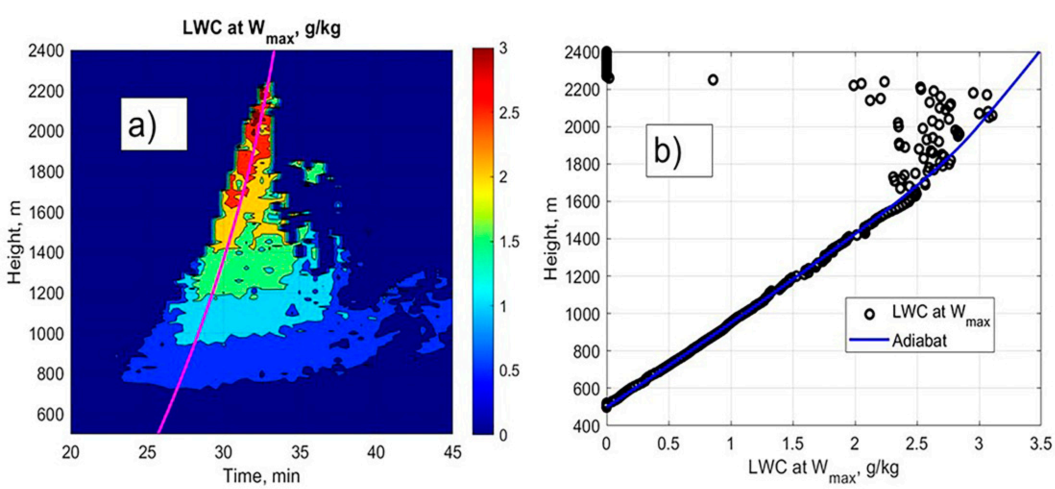

FIG. 7. (a) Height–time field of $q_{l\_max}(z, t)$. The magenta line (the same line as in Fig. 6a) shows z–t trajectory of the point parcel rising at maximum velocity. (b) Profile of LWC along the trajectory of the point parcel. The adiabatic profile of LWC_{ad} is shown by blue.

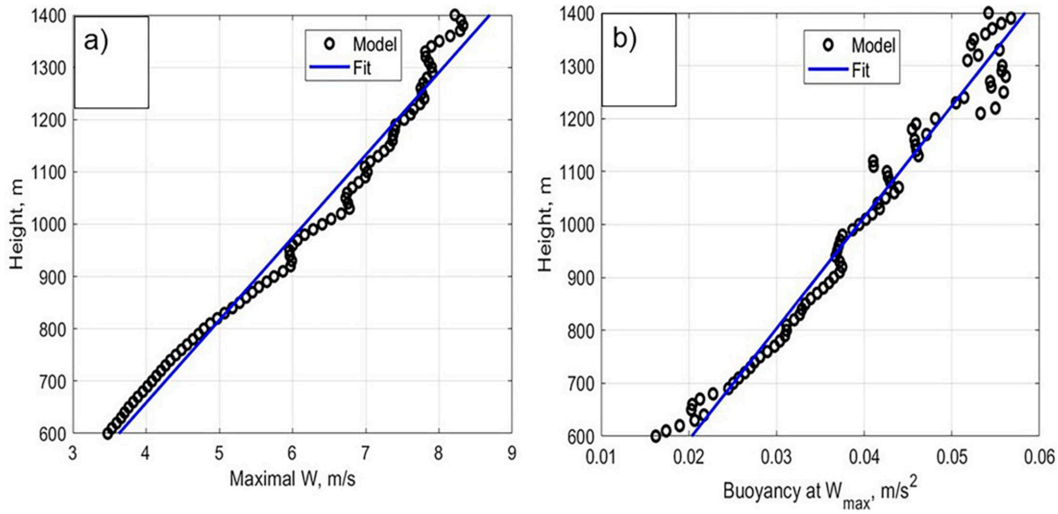

FIG. 8. Height profiles of (a) the point parcel velocity (circles) and its linear approximation (blue line) and (b) the buoyancy acceleration (circles) and its linear approximation (blue line).

adiabatic LWC profile shown in Fig. 7b (the algorithm of profile calculation is described in appendix A). The linear increase of LWC with height takes place up to 1600 m, and then the LWC at the point of the maximum updraft velocity deviates from the adiabatic value. However, the small separate volumes with LWC close to the adiabatic one, exist up to the maximum cloud top (2200 m). These volumes, though, do not coincide with the points of the maximum updraft velocity.

The coincidence of the LWC profile with the adiabatic one means adiabaticity of the core. In our case, the core is observed up to about 1600–1800 m. It means that the cloud core supported with undiluted air from the cloud base is not affected by friction caused by entrainment of calm air. The quasi-horizontal bands of identical LWC in the points of maximum velocity seen in Fig. 7a indicate that the cloud core with high adiabatic fraction (AF) exists for ~15 min at low levels (below 1200 m), but rapidly dissipates at high levels (above ~1600 m). Figures 6a and 7a show that cloudy air also exists above the head bubble. After ascending of the head bubble, the air with adiabatic LWC continues ascending in the tail of the starting plume, but at lower maximum velocity.

In several in situ observations of small Cu the maximum values of LWC become lower than the adiabatic values at about 1/5 of cloud depth from cloud base (e.g., Gerber et al. 2008). The model shows the existence of volumes with high AF at higher levels than it is reported in observations. According to results of LES (Khain et al. 2019; Eytan et al. 2022), the area fraction of volumes with AF $>$ 0.8–0.9 decreases as height increases, and is as low as 1% near the cloud top (around 1800 m). The time period during which such volumes exist is about one minute. Due to very low occurrence of volumes with high AF at high levels, especially very close to cloud top, such volumes may not be registered in aircraft measurements along separate traverses. At the same time, the model statistics is by several orders of magnitude larger than that used in any in situ measurements, and the model registers all such volumes. In addition, analysis of in situ observations allowed Blyth et al. (1988) to conclude that rapid mixing of undiluted air and entrainment air takes place near cloud top, so that "the infrequent observations of undilute air may be because most cloud observations are made too late in the cloud's lifetime." Note that the comparison of observations with simulations is a quite complicated problem because of differences in time, locations, as well as just certain errors in both measurements and simulations. These errors are especially pronounced when the comparison in zones of very high relative humidity takes place, where small fluctuations can lead to change of LWCad by several percent. Note also that the difference in the values of LWCad and AF can be caused also by difference in methods of the calculation of these quantities (Eytan et al. 2021).

It is of interest that despite the negligible probability to detect air volumes with high AF near tops of Cu, some high-frequency measurements show the existence of such volumes with AF $>$ 0.7 within small Cu (Gerber 2000; Wendish and Brenguier 2013). Some observations (Jensen et al. 1985; Konwar et al. 2021) also reported the existence of undilute parcels.

Now we would like to emphasize that the lower part of the maximum velocity profile shown in Fig. 6b is close to linear dependence, at least up to the height of the beginning of the inversion layer, that is, up to 1400 m (Fig. 1). The mean square linear approximation of the profile is shown in Fig. 8a. The quality of approximation is characterized by the high value of correlation coefficient R = 0.9901. Using Eq. (2), we also calculate buoyancy acceleration profile at the same points as those used in the maximum velocity profile calculations. This profile is also well approximated by linear function, as is shown in Fig. 8b (the correlation coefficient is R = 0.9846).

The linear high-quality approximations can be written (we suppose that $z_0 = 600$ m is the height of cloud base)

$$W_{\max}(z) = 6.33 \times 10^{-3}(z - 600) + 3.630, \quad (10)$$

$$B(z) = 4.75 \times 10^{-5}(z - 600) + 2.033 \times 10^{-2}, \quad (11)$$

where z is in meters, $W_{\max}(z)$ is in meters per second, and B is in meters per squared second. The fact that the height profiles of both $W_{\max}$ and B are linear means that there is a linear dependence between $W_{\max}$ and B, which is valid at least up to the height of 1400 m. The approximation formula for this dependence is

$$W_{\max}(B) = 130.25 \times B + 1.037; \quad (12)$$

$W_{\max}$ is not equal to zero when $B = 0$. This is due to the presence of initial artificial temperature pulse, which acts during some time to trigger the cloud development. This velocity, which is equal to $W_0 = 1.037$ m s^{-1}, should be subtracted from $W_{\max}$ in the parcel model formula.

The linearity of the dependencies, along with the fact that the adiabatic core is not affected by friction, makes it possible to describe the maximum updraft in the cloud core by a generalized parcel model with the dynamic equation analogous to Eq. (4):

$$(W_{\max} - W_0)\frac{dW_{\max}}{dz} = c_1 B(z). \quad (13)$$

The coefficient in this equation can be obtained from the approximating dependences [(10) and (11)] is

$$c_1 = 0.82. \quad (14)$$

The value of c_1 is close to the value of the corresponding coefficient in Eq. (1) where it is evaluated equal to approximately 0.67. This coefficient is related to the ratio of so-called induced mass to the mass of the parcel and was approximately estimated by Turner (1963) following the theory of ascending bubbles. It is hardly possible to expect a better agreement in the values of the coefficient evaluated using the results of LES in real clouds where complicate microphysical processes take place, and values obtained in simplified considerations or in laboratory experiments of jets.

Thus, the points of the maximum updraft velocity on z–t trajectory can be considered belonging to a rising accelerating point parcel. The point parcel obeys the motion Eq. (13), and LWC in it obeys the adiabatic dependence. The volume at maximum velocity is not affected (or is affected only slightly) by entrainment from the cloud boundaries.

There are several important conclusions from the results reported above. Entrainment has a negligible effect on $W_{\max}$ (at least for Cu with cloud tops up to 1800–2000 m). The existence of the small undiluted volume in Cu core is extremely important. This volume is maximally buoyant and determines the cloud-top height, so its existence is crucial for the entire cloud structure. If convective motions form "a skeleton" of the cloud, the undiluted volume associated to the cloud core plays the role of "the backbone" of this skeleton. Also, the existence of the undiluted core indicates a strong horizontal inhomogeneity of the cloud, which in turn indicates significant limitations of cloud models based on the concept of a horizontally homogeneous bubble or jet. The serious limitations of this concept applied in 1D cloud models were discussed earlier, e.g., by Houze (2014).

5. Characteristics of the cloud updraft zone

a. Main definitions

It is clear that clouds are not horizontally homogeneous, in contrast to an ascending horizontally homogeneous bubble or jet considered in parcel models. Now we are going to compare the behavior of the CUZ determined by the condition $W > 0.1$ m s^{-1} and $q > 0.01$ g kg^{-1} with the behavior of an equivalent bubble or jet whose width is equal to the CUZ width. For this purpose, we surround the point of the maximum vertical velocity with a boundary in the horizontal plane, as shown in Fig. 2. The size and square of the area surrounded by the boundary (the size and cross-sectional area of the CUZ) change with time and height. The time and height dependence of the mean square radius $R(z,t) = \sqrt{S(z,t)/\pi}$, where $S(z, t)$ is the area, is shown in Fig. 9a. One can see that the radius of the CUZ decreases with height, from ~320 m down to 150 m. This decrease contradicts in some way to the jet model, according to which the radius of a jet should increase linearly with height (Pruppacher and Klett 1997). The decrease above 1400 m is likely related to the effect of the inversion layer and formation of the subsiding shell. Along $z - t$ trajectory, in the height range below the inversion level (600–1400 m), this decrease is insignificant (Fig. 9b) so it can be assumed that $R \approx 304$ m is the constant radius.

We now consider the behavior of different quantities characterizing the CUZ, including the mass fluxes inflowing in the CUZ both laterally and from below. Instead of maximal vertical velocity and other quantities at points of the maximum updraft velocity we are using the values averaged over the CUZ area referred here as to top-hat values. We will again use the z–t trajectory of the corresponding point parcel, described in section 4, as the trajectory of a broad head bubble. We will use the quantities averaged along the lateral boundary of the CUZ as environment values. Mass fluxes through the boundary will be averaged at the same way.

b. Dynamical characteristics of the cloud updraft zone

Contours of the top-hat updraft velocity in height–time space $\overline{W}(z,t)$ and the vertical profile of this velocity along z–t trajectory are shown in Fig. 10. Comparison with Fig. 6 shows that the top-hat velocity is 3 times less than the maximum velocity $W_{\max}(z, t)$. As in the case of the point parcel, $\overline{W}(z,t)$ does not behave like a stationary vertical jet, which is seen because the absence of horizontal bands on the contours of $\overline{W}(z,t)$ in Fig. 10a. Therefore, the CUZ structure resembles the starting plume: a nonstationary jet capped by a head bubble during the developing stage (Houze 2014). This result agrees with the conclusions made by McCarthy (1974). It is

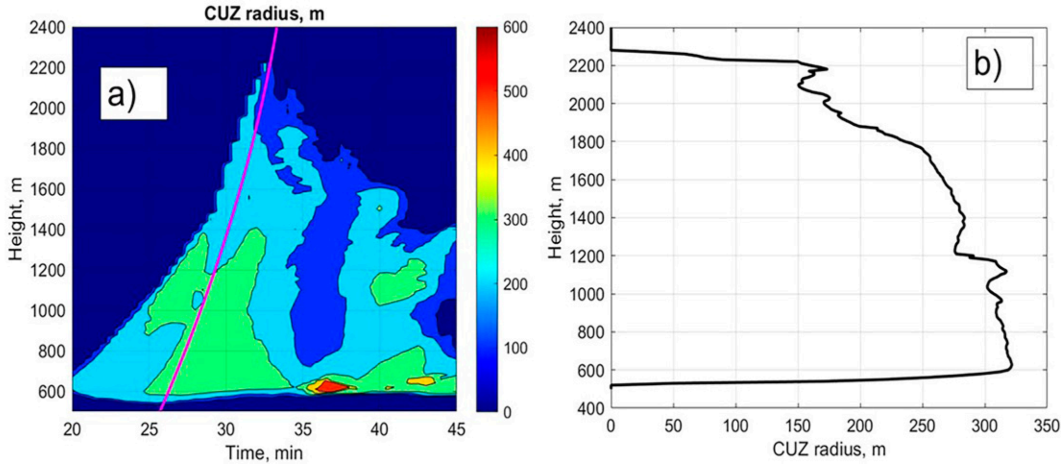

FIG. 9. (a) Height–time field of the CUZ radius $R(z, t)$. The magenta line shows z–t trajectory of the corresponding rising point parcel. (b) Vertical profile of the CUZ radius along the trajectory of the point parcel.

noteworthy that the starting plume associated to the CUZ ascends slower than the point parcel ascending at the maximum velocity.

An increase of the top-hat updraft velocity stops at the height of 1400 m, i.e., at the lower level of the inversion layer, and then the updraft velocity decreases because of the influence of negative buoyancy force. The latter is seen in the Fig. 11, which demonstrates that the top-hat buoyancy changes the sign from positive to negative at $z = 1500$ m. In Fig. 10a the lower part of the cloud demonstrates some deviation of the point parcel trajectory from the trajectory of the broad head bubble. It can be explained by absence of central symmetry of the CUZ. Nevertheless, we will assume, for the sake of comparison, that both the point parcel and the head bubble move along the same trajectory.

Like in the case of the point parcel, the vertical profiles of the top-hat vertical velocity $\overline{W}(z)$ and the top-hat buoyancy $\overline{B}(z)$ in the lower part the of cloud can be approximated by linear dependences with a good accuracy (Fig. 12). The corresponding correlation coefficients characterizing quality of the fits are $R = 0.9762$ for $\overline{W}(z)$ and $R = 0.94$ for $\overline{B}(z)$. The linear fit dependences have the forms

$$\overline{W}(z) = 2.678 \times 10^{-3}(z - 600) + 1.117 \quad (15)$$

and

$$\overline{B}(z) = 2.11 \times 10^{-5}(z - 600) + 2.537 \times 10^{-3}. \quad (16)$$

In Eqs. (15) and (16) z is in meters, $\overline{W}(z)$ is in meters per second, and $\overline{B}$ is in meters per squared second.

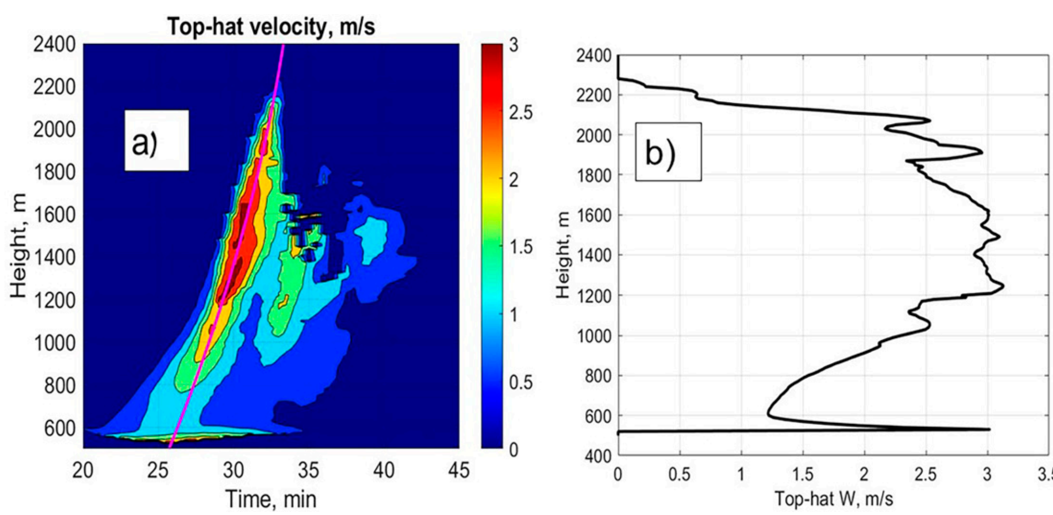

FIG. 10. (a) Height–time field of top-hat vertical velocity of CUZ $\overline{W}(z,t)$. The magenta line shows z–t trajectory of the corresponding rising point parcel. (b) Vertical profile of the top-hat velocity of the head bubble. The initial artificial pulse of the vertical velocity, which acts during some time to trigger the cloud development, is seen in the lowest part of the figure.

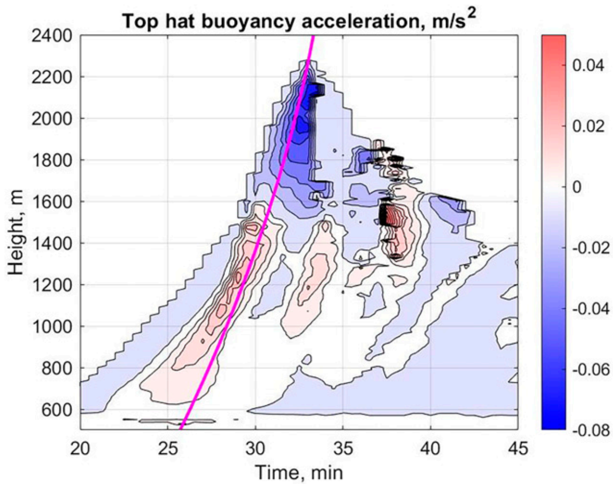

FIG. 11. Height–time field of the top-hat buoyancy acceleration $\overline{B}(z,t)$. The magenta line shows z–t trajectory of the corresponding rising point parcel.

In the process of ascent, the head bubble experiences friction force, which arises due to the difference in the velocities in the head bubble and penetrating surrounding air. Dynamical entrainment (convective inflows across the lateral border of the CUZ) and dynamical detrainment (convective outflows across the lateral border of the CUZ) are the results of the flow continuity and pressure fluctuations. An example of the horizontal velocity vectors at the CUZ boundary is shown by arrows in Fig. 2. It is seen that some vectors are directed inside the core and some vectors are directed outside. Influxes of different thermodynamic and microphysical quantities influence the motion and structure of a rising head bubble, whereas outfluxes change the properties of the air around the head bubble (Houze 2014). Since we initially filtered out turbulent fluctuations of velocity components (section 2b), in this study we analyze the influence of dynamical entrainment only.

Dynamical entrainment is usually characterized by entrainment rate E, whereas dynamical detrainment is characterized by detrainment rate D. In accordance with the continuity equation, these rates are related to the flux of vertical velocity as (Pruppacher and Klett 1997; Houze 2014)

$$E - D = \frac{1}{\Phi_z}\frac{d\Phi_z}{dz}, \tag{17}$$

where Φ_z is the flux of vertical velocity through the horizontal cross section of the CUZ, directed from bottom to top. This flux is equal to the product of the vertical top-hat velocity and the area of the CUZ, written as $\Phi_z = \int_S \overline{W}\, dS = \overline{W}(z,t)S(z,t)$. The vertical gradient of Φ_z is equal to the difference of influx of the horizontal velocity through the contour of the horizontal boundary $\oint_l V_{R+}\, dl$ and the corresponding outflux $\oint_l V_{R-}\, dl$, where V_{R+} and V_{R-} are the radial velocity directed inside the CUZ and outside the CUZ, respectively. Fluxes E and D are calculated at every height level.

The contours of the entrainment rate in the height–time space $E(z, t)$ and the vertical profile of the entrainment rate along z–t trajectory $E(z)$ are shown in Fig. 13. One can see that dynamical entrainment rate at any height reaches its maximum values in 2–3 minutes after the head bubble passed through the height levels. Thus, dynamical entrainment from lateral boundaries strongly affects the jet in the tail of the starting plume but not the head bubble. The typical (averaged value) of the entrainment rate is ~10^{-3} m^{-1}, which agrees with evaluations made by Stommel (1951). The maximum value of the entrainment rate along z–t trajectory equal to 1.7×10^{-3} m^{-1} is reached at z = 950 m. This dynamical entrainment rate corresponds to entrainment

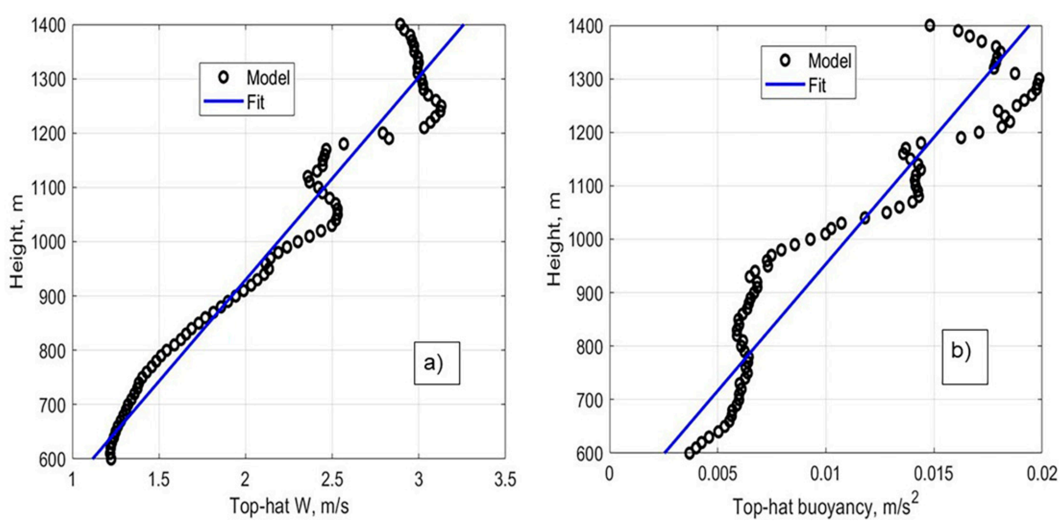

FIG. 12. Height profiles of (a) the top-hat velocity (circles) and its linear approximation (blue line) and (b) the top-hat buoyancy acceleration (circles) and its linear approximation (blue line).

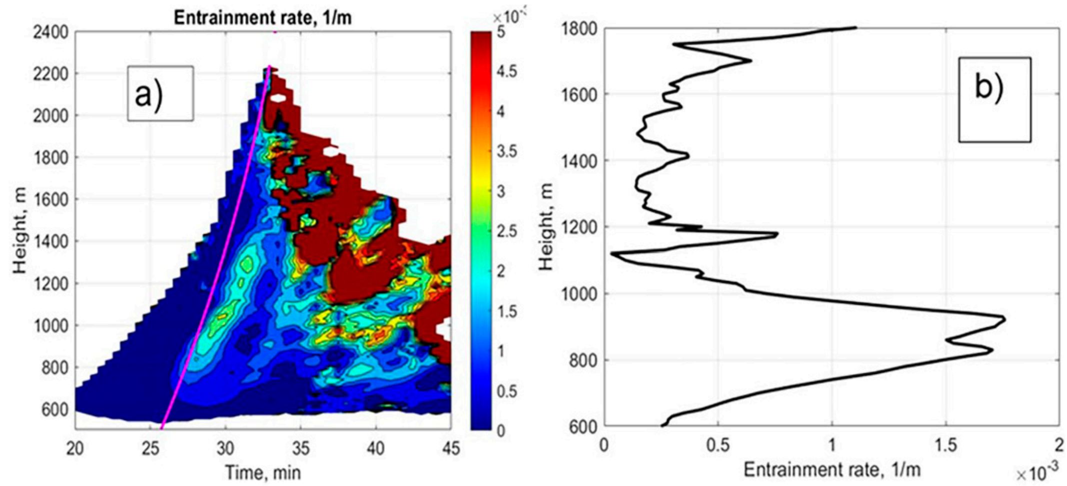

FIG. 13. (a) Height–time field of dynamical entrainment rate $E(z, t)$. The magenta line shows z–t trajectory of the corresponding rising point parcel. (b) Vertical profile of dynamical entrainment rate into the head bubble.

parameter $\mu = E/R = 0.54$, which is close to 0.6 (the value given by Houze 2014).

To evaluate the role of a friction-like force on the head bubble motion, we compare the acceleration profile equal to $E(z)[\overline{W}(z) - \overline{W}_0]^2$ with the buoyancy acceleration profile. Both profiles are calculated along z–t trajectory corresponding to maximum updraft velocity $W_{\max}$. Figure 14 shows the height profiles of the top-hat buoyancy acceleration, and of the absolute value of friction acceleration [the second term on the right-hand side of Eq. (4)] within the height range of 600–1400 m. One can see in lower part of the profiles the buoyancy is 4–7 times larger than the friction. In upper part of the profiles, the buoyancy is by an order of magnitude larger than the friction term. This finding makes it possible to neglect the last term in the motion Eq. (4) and, using the fit

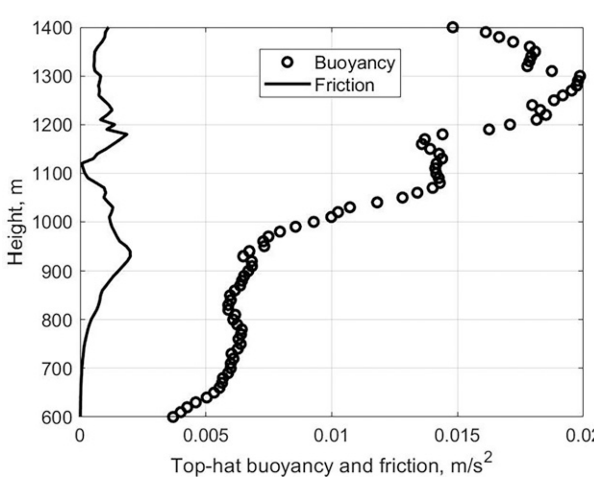

FIG. 14. Vertical profiles of top-hat buoyancy acceleration (circles), and absolute value of friction-like acceleration caused by dynamical entrainment (solid line).

equations, to write down the motion equation in the linear form similar to Eq. (13) for the point parcel

$$(\overline{W} - W_0)\frac{d\overline{W}}{dz} \approx c_1\overline{B}(z), \qquad (18)$$

With coefficient $c_1 = 0.34$ and the initial velocity $W_0 = 0.795$ m s^{-1}. Equation (18) can be considered a dynamical part of a parcel model, which can be applied at the developing stage of Cu evolution.

The results obtained indicate that the decrease in the top-hat vertical velocity of the starting plume, as compared with that of the point parcel velocity, is not caused by the dynamic friction-like effect of entrainment, but by a decrease in the top-hat buoyancy. This finding clearly contradicts with most parcel model-based convective parameterizations in which updraft velocity and cloud height are fully determined by the entrainment parameter (e.g., Arakawa and Schubert 1974; Plant and Yano 2015). The negligible role of the entrainment term in the dynamical parcel equation was also reported by de Roode et al. (2012). In that study it was found that "a parameterization for the damping of the in-cloud vertical velocity by an entrainment term seems misleading." De Roode et al. (2012) attribute the decrease in $\overline{W}(z)$ to effects of the pressure gradients.

c. Fluxes of conservative thermodynamic quantities

In the previous subsection it was shown that the entrainment term is not responsible for the decrease in the top-hat vertical velocity of the head bubble in starting plume. Now we consider the budget equations for quantities conservative in moist adiabatic processes, namely, the top-hat total water mixing ratio $\overline{q}_t(z)$ and the top-hat liquid water potential temperature $\overline{\theta}_l(z)$. Since the total water mixing ratio in the environment air is lower, while the liquid water potential temperature is higher than that in the CUZ, mixing with environment air should decrease $\overline{q}_t(z)$ and increase $\overline{\theta}_l(z)$. The

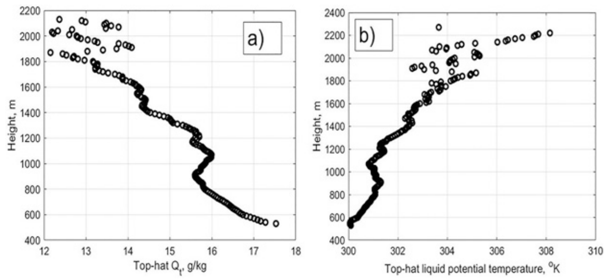

FIG. 15. Vertical profiles of (a) the top-hat total water mixing ratio $\overline{q}_t(z)$ and (b) the top-hat liquid water potential temperature $\overline{\theta}_l(z)$ along z–t trajectory of the rising point parcel.

main question to answer is, "Can the entrainment terms in Eqs. (7) and (8) explain the changes of $\overline{q}_t(z)$ and $\overline{\theta}_l(z)$, simulated by LES?"

The height profiles of the top-hat total water mixing ratio $\overline{q}_t(z)$ and the top-hat liquid water potential temperature $\overline{\theta}_l(z)$ along z–t trajectory of the corresponding rising point parcel are shown in Fig. 15. These profiles were calculated using Eqs. (5) and (6). Figure 15 shows that $\overline{q}_t(z)$ linearly decreases with height within the height range of 600–1600 m, while $\overline{\theta}_l(z)$ increases from 300 K at $z = 500$ m up to 303 K at $z = 1600$ m, in agreement with the signs of the entrainment terms.

Profiles of the entrainment terms of Eqs. (7) and (8) along z–t trajectory are shown in Fig. 16. In the calculations, entrainment rate E is taken from Fig. 13, and quantities $\tilde{q}_t$ and $\tilde{\theta}_l$ are calculated as mean values at CUZ boundaries, corresponding to influx from the subsiding shell. The θ_l term profile (Fig. 16b) resembles the profile of entrainment rate shown in Fig. 13b, while the q_t term profile (Fig. 16a) resembles its mirror image. We can compare the values of the displayed quantities with the corresponding values of derivatives on the left-hand side of Eqs. (7) and (8). These derivatives, evaluated using average slopes of the corresponding height profiles within the range of 600–1600 m (Figs. 15a,b), are equal to -0.003 g kg^{-1} m^{-1} and 0.0025 K m^{-1}, respectively, as shown in Figs. 16a and 16b. Comparison of these values with the profiles of the corresponding entrainment terms leads to the conclusion that dynamical lateral entrainment is not the main reason of changes in $\overline{q}_t(z)$ and in $\overline{\theta}_l(z)$ changes.

The results shown in Figs. 14 and 16 lead to unexpected (and somehow paradoxical) conclusion that dynamical entrainment cannot lead to the changes of W, q_t, and θ_l, obtained in LES. Indeed, as it was shown above, entrainment through the CUZ boundary is significant in the tail behind (i.e., below) the ascending head bubble, but not in the bubble itself. It suggests that, besides entrainment, there exists another mechanism responsible for the decrease of q_t, the increase of θ_l, and likely, the decrease of buoyancy.

d. LWC inside CUZ and adiabatic fraction

The height–time field of the top-hat LWC $\overline{q}_l(z,t)$ (Fig. 17a) is significantly different from the field of maximum LWC $q_{l\_\max}(z, t)$ in the point parcel, shown in Fig. 7a. Comparison of Figs. 7 and 17 shows that $\overline{q}_l(z,t)$ is maximum along the trajectory of the point parcel. At the same time, $\overline{q}_l(z,t)$ is smaller than the adiabatic LWC at all height levels and time instances. The top-hat AF along z–t trajectory can be estimated by Fig. 17b. Since dependence $\overline{q}_l(z)$ demonstrates a linear increase within the height range of 600–1600 m, similar to the adiabatic profile $q_{\rm ad}(z)$, the ratio $\overline{\rm AF}(z) = \overline{q}_l(z)/q_{\rm ad}(z)$ is approximately constant and equal to 0.4–0.6. This value is in accordance with previously obtained measurement results (Gerber et al. 2008; Katzwinkel et al. 2014). The second significant difference between the CUZ and the cloud core is nonstationarity of LWC, that is, a rapid decrease of $\overline{q}(z,t)$ in time at any altitude (there are no extended horizontal bands of the constant LWC contours, which are seen in Fig. 7a).

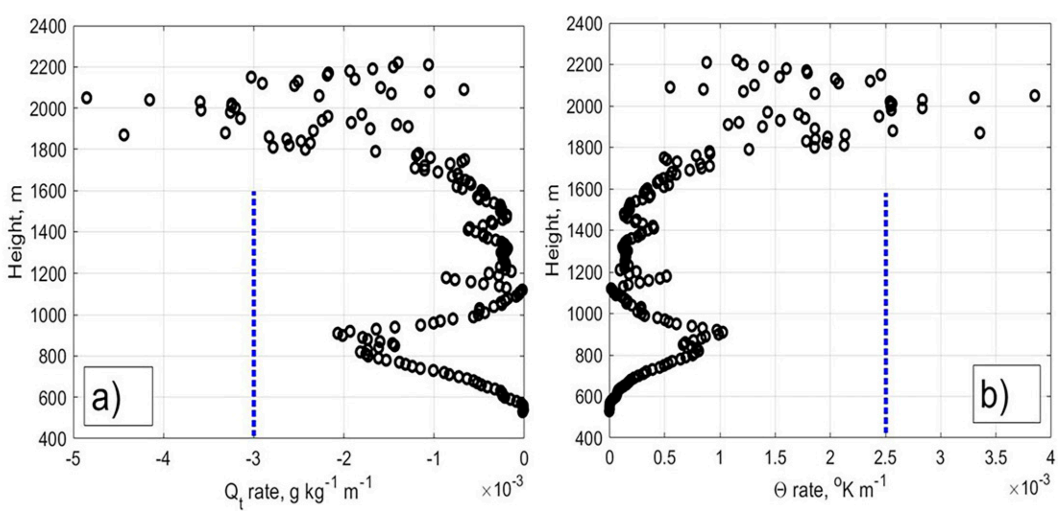

FIG. 16. Vertical profiles of (a) the entrainment terms of q_t in Eq. (7) and (b) the entrainment terms of θ_l in Eq. (8) along z–t trajectory of the rising point parcel. The values of average slopes of the height profiles $d\overline{q}_t/dz$ and $d\overline{\theta}_l/dz$ within the range of 600–1600 m are shown by dashed vertical lines.

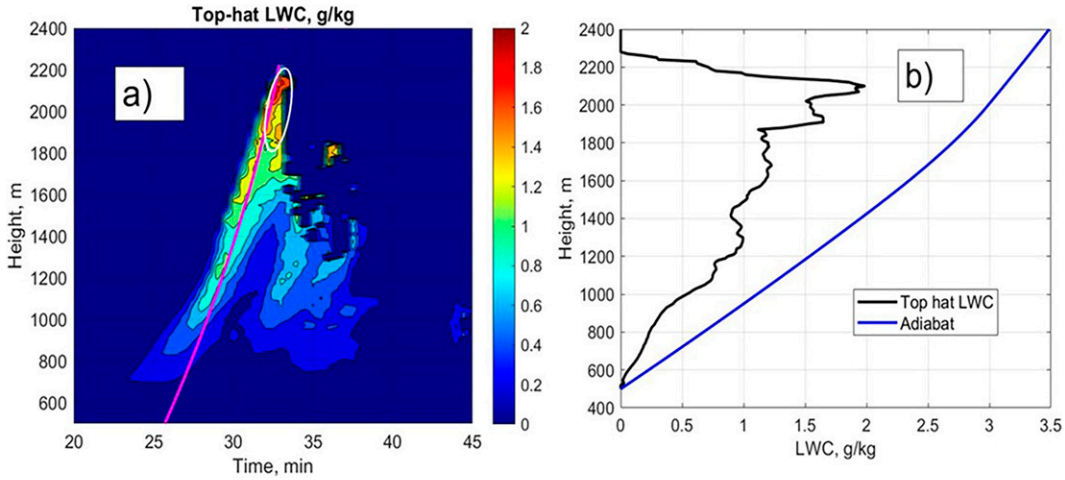

FIG. 17. (a) Height–time field of $\overline{q}_l(z,t)$. The magenta line shows z–t trajectory of rising point parcel. The white ellipse near the cloud top shows the zone of rapid LWC formation. (b) Vertical profile of top-hat LWC along the trajectory of point parcel. The adiabatic profile is marked blue.

One of the reasons for both the decrease and nonstationarity of LWC in time is the continuous mixing between the air in the CUZ across the lateral boundary with the air surrounding of the CUZ. The fact that the LWC decrease is related to the entrainment is well seen from the comparison of LWC decrease zone in the height–time fields in Fig. 17a at $t = 30$–35 min and $z < 1400$ m, to the zone of strong entrainment in height–time fields in Fig. 13a at $t = 28$–33 min, and $z < 1400$ m. The strong decrease in LWC in Fig. 17a (from ~1 g kg^{-1} to ~0.2–0.4) occurs 2 min after a strong entrainment event. Entrainment decreases LWC a few minutes after the passing the ascending head bubble with maximum LWC. As a result, there is the decrease in LWC in the tail of the starting plume. In terms of the entire cloud, this result shows that dynamical lateral entrainment decreases LWC a few hundred meters below the cloud top. Also, the top-hat LWC ascends at nearly the same speed as the point parcel, as is well seen in Fig. 6 and in Fig. 17a. Indeed, the top-hat LWC arises during ~1 min (the white ellipse in Fig. 17a), and $\overline{q}_l(z,t)$ gets the maximum value. At the same time, $\overline{q}_l(z,t) < q_{\mathrm{ad}}$ near the cloud top (Fig. 17b), despite the fact that the entrainment rate is not high at these altitudes (Fig. 13b).

The following consideration allows us to relate the top-hat LWC in the CUZ with W and AF. Both the updraft velocity and the LWC decrease from the center of a rising head bubble toward its lateral boundaries (appendix B). The vertical distances traveled by different cloudy volumes inside the CUZ reaching the same height at the same time instance are different decreasing from center of CUZ to its boundaries. A simplified scheme of the process is given in Fig. 18. The air volumes penetrating the CUZ due to dynamical entrainment begin ascending from different levels $z_0(r)$ at velocities allowing to reach the same level z at the same time instance t. The air ascending from the cloud base forms adiabatic core, since entrainment does not affect the core. The air entering the CUZ above cloud base mixes with the cloud air and becomes saturated. The amount of LWC accumulated inside individual volumes in the CUZ is proportional to distances $z - z_0(r)$, according to the equation of condensational growth. As a result, the LWC decreases with the increase in the distance from the center of the CUZ, leading to the deviation of top-hat AF in CUZ from one.

Suppose the vertical velocity inside the CUZ changes with the height z and decreases with the distance from the center of the CUZ r, according to formula

$$W(r,z) \approx W_{\max}(z)\left[1 - \left(\frac{r}{\overline{R}}\right)^{\beta}\right], \tag{19}$$

where $W_{\max}(z)$ is the profile of the vertical velocity at the head bubble center (i.e., in the point parcel, Fig. 6b), $\overline{R}$ is the mean radius of the CUZ, and exponent β being independent of r characterizes the rate of vertical velocity decrease in the radial direction. In this case, the top-hat adiabatic fraction can be estimated as (appendix B)

$$\overline{\mathrm{AF}}(z) \approx \frac{\beta(z)}{[2 + \beta(z)]}. \tag{20}$$

In case $r = \overline{R}$ (the edge of the CUZ), $\beta = 0$ and $\overline{\mathrm{AF}}(z) = 0$; in case the vertical velocity is uniformly distributed (i.e., when the entire air ascents from the cloud base), and $\beta \to \infty$ in the cross section of the CUZ, and $\overline{\mathrm{AF}}(z) \to 1$. The linear radial profile of the vertical velocity corresponds to $\beta = 1$ and $\overline{\mathrm{AF}} = 0.33$, while the parabolic profile corresponds to $\beta = 2$ and $\overline{\mathrm{AF}} = 0.5$.

Equation (20) was obtained under the assumption that the individual volumes inside the CUZ reaching the same height at the same time instance were initially saturated and do not contain any significant liquid water. This assumption is discussed in section 6. An example of approximation of the

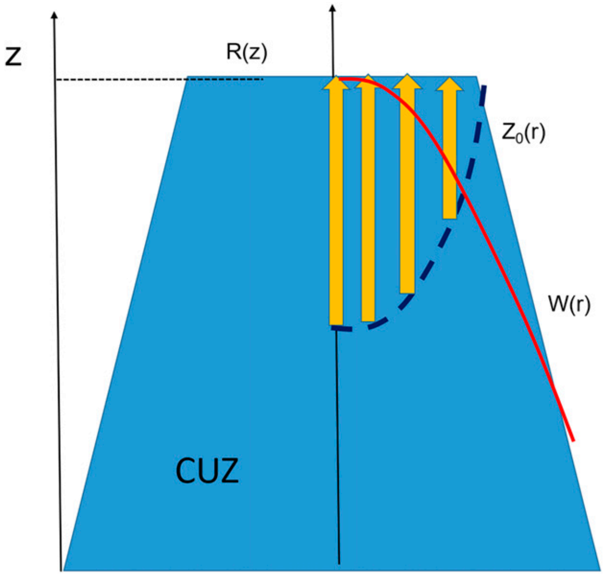

FIG. 18. Scheme illustrating estimation of the adiabatic fraction in CUZ. The air volumes rise inside CUZ along moist adiabats with different vertical velocities from different altitudes $z_0(r)$ (dashed black line) to reach the same altitude z at the same time t. The ascent is shown by yellow arrows. The profile of $W(r)$ is shown by red curve.

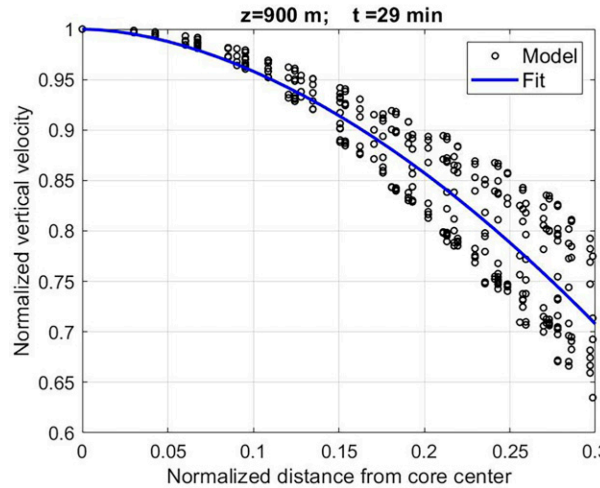

FIG. 19. An example of approximation of the dependence $W(r)$ by means of using Eq. (19). The value of exponent β is close to 2 in this case, which corresponds to adiabatic fraction of 0.5.

dependence $W(r)$ using Eq. (19) is shown in Fig. 19. The example point was chosen close to z–t trajectory of the rising point parcel below the inversion level. The value of exponent β is close to 2 in this case, which corresponds to value of 0.5 of the adiabatic fraction.

In Fig. 20 we compare the top-hat adiabatic fraction along z–t trajectory, calculated as a ratio of two profiles shown in Fig. 17b and the profile, estimated using model Eq. (20). The characteristic values of the adiabatic fraction in both evaluations fluctuate around the value of 0.5, which, as mentioned above, is a typical value measured in small Cu. Fluctuations of the model adiabatic fraction can be caused by different reasons such as size changes of the CUZ, direct influence of entrainment and mixing, asymmetry in detrainment from the CUZ, etc. However, the good agreement of the mean values of the adiabatic fraction might explain why AF is less than one in the CUZ. It may be due to the difference in liquid water accumulation in air volumes rising over different distances up to the same height level including the level of cloud top. In more detail, this phenomenon is analyzed in section 6 and appendix B.

The scheme in Fig. 18 illustrates formation of the radial profile of LWC, $q_l(r)$, as a set of small cloudy volumes adiabatically ascending from different initial levels. The ascent takes place without any turbulent mixing between these volumes. It is of interest to analyze the possible effects of in-cloud turbulent mixing on the radial LWC profile. The schemes of $q_l(r)$ formation without and with the horizontal mixing effect are shown in Figs. 21a and 21b, respectively.

Droplet evaporation during mixing takes place in the vicinity of the cloud edge, where relative humidity of the entrained air parcels RH < 100%. The width of such interface zone varies from several tens of meters to ~100 m (Gerber et al. 2008; Konwar et al. 2021; Khain and Pinsky 2018). As soon as RH in the entrained volumes becomes close to 100%, mixing is not any longer accompanied by droplet evaporation, and droplets during horizontal mixing behave like a passive scalar. So neighboring volumes exchange droplets, retaining the same RH total droplet mass, and number concentration.

Figure 21a corresponds to the scheme in Fig. 18 where mixing is absent. Two volumes ascend from different initial levels

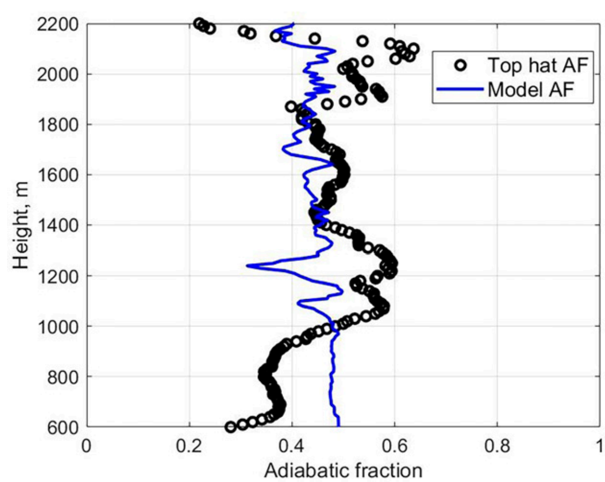

FIG. 20. Comparison of the top-hat adiabatic fraction profile calculated as a ratio of two profiles shown in Fig. 17b, and the profile estimated using model Eq. (20) along z–t trajectory of rising point parcel.

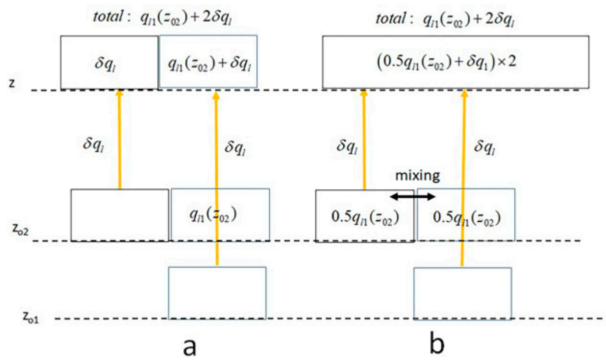

FIG. 21. A scheme of LWC(r) formation (a) without mixing and (b) with mixing. It is shown that mixing does not affect the mean LWC at level z.

z_{01} and z_{02}, and finally reach the level z at the same time. The values of LWC at the initial levels are assumed to be zero (empty squares). The initial levels can be considered as the levels of the air volume entrainment. Assuming adiabatic ascent, we conclude that LWC values at level z in the parcels are δq_l and $q_l(z_{02}) + \delta q_l$, where δq_l is the LWC increase during the ascent from z_{02} to z. In case there is mixing of these air volumes (assumed equal for simplicity) (Fig. 21b), the LWC values in both volumes at z_{02} are equal to $(1/2)q_l(z_{02})$. The LWC increases in each volume by δq_l. Thus, at the level z the total LWC is the same for both in in-cloud mixing and no-mixing cases, which leads to the same top-hat LWC and AF. In case the in-cloud mixing is not very strong, it cannot, therefore, affect the horizontal profile of LWC anyhow significantly.

It should be noted that the schemes in Fig. 21a and 21b are simplified and do not take into account the condensation/evaporation effects in the process of horizontal mixing.

6. Discussion and conclusions: Possible impact of Hill's vortex at cloud top

In Part I of the study (Pinsky et al. 2021) we showed that it is possible to separate in-cloud air motions into two large groups: convective motions responsible for directed mass transport, and turbulent motions whose effect is likely to be associated to diffusion processes. We supposed that convective motions with scales on the order of a cloud size form a cloud "skeleton." In this Part II of the study we aimed at clarifying the extent to which a real complex cloud simulated by 10-m-grid-spacing LES can be described by low parametric parcel models in which mass transport and entrainment are of convective nature. In such parcel models, some turbulence effects are considered indirectly, via the assumption that clouds are horizontally homogeneous.

We performed simulations of a nonprecipitating trade wind Cu growing under BOMEX conditions. The simulations were carried out using SAM with spectral bin microphysics. To investigate the cloud dynamics with scales larger than turbulence scales, the modeled fields of air velocity in the cloud were filtered by a wavelet filter in order to separate the analyzed convective flows from turbulent flows. In this way the spatial–time variations of cloud updraft zone (CUZ) became distinct. The concept that cloud at the developing state can be represented by bubble or a jet (which means applicability of the parcel models for simulating a convective cloud) was tested. The LWC fields inside CUZ was also analyzed.

Two types of objects in a developing convective cloud were investigated: a small volume ascending at maximum velocity (a point parcel) and the CUZ determined by conditions $W > 0.1$ m s^{-1}, and $q_l > 0.01$ g kg^{-1}. The point parcel was located within the CUZ. It was found that the point parcel representing the cloud core is adiabatic up to the height of 1800 m. The air in this parcel ascends from the cloud base and determines the cloud-top height. The top-hat values of the updraft velocity in CUZ, and adiabatic fraction in CUZ are substantially lower than those at in the point parcel. The results show that small volumes with adiabatic LWC exist up to the maximum cloud height of about 2200 m.

The individual terms in the equations typically used in parcel models were evaluated taking into account the results of LES. It is shown that a cumulus cloud can be reasonably represented by a starting plume model, at least up to the heights of the inversion layer (in our case, up to 1400–1500 m). Dynamically, the CUZ of a developing cloud resembles starting plume consisting of a head bubble with a tail of nonstationary jet. The equivalent radius of this bubble varies slightly with altitude and ranges between 150 and 300 m. Both the top-hat vertical velocity and the buoyancy acceleration linearly increase with the height up to the inversion layer.

An important finding of this study is that lateral dynamical entrainment into an individual Cu has a little effect not only on a point parcel ascending with the maximal $W_{\max}$, but also on the top-hat velocity, as well as on the changes in the top-hat conservative variables $\overline{q}_t$ and $\overline{\theta}_l$. The negligible effect of lateral entrainment on vertical velocity was previously found by de Roode et al. (2012), who analyzed large groups of clouds generated by LES. This fact shows that a widely used convective parameterization approach where the entrainment parameter is varied to control $\overline{W}$, mass flux, and cloud-top height is not well grounded and should be tested by LES.

As in many previous studies (e.g., Houze 2014), it was found that the assumption of horizontal homogeneity of clouds used in parcel models is too crude. On the contrary, horizontal inhomogeneity makes it possible to explain the relationship between vertical velocity, LWC, and adiabatic fraction (AF) in CUZ. According to this process, mixing of cloudy air volumes with surrounding air leads to droplet evaporation and establishing of saturation condition in CUZ. Then the saturated air volumes ascend adiabatically inside CUZ up to a certain level, passing a certain distance, depending on the radial distribution of vertical velocity $W(r)$ and absorb certain amounts of water vapor. Reaching this level, they form the realistic radial profiles of LWC in the vicinity of the ascending cloud top, and the realistic vertical profile of top-hat AF. This result stresses again the important role of convective-scale motions as compared to turbulent motions in formation of cloud structure.

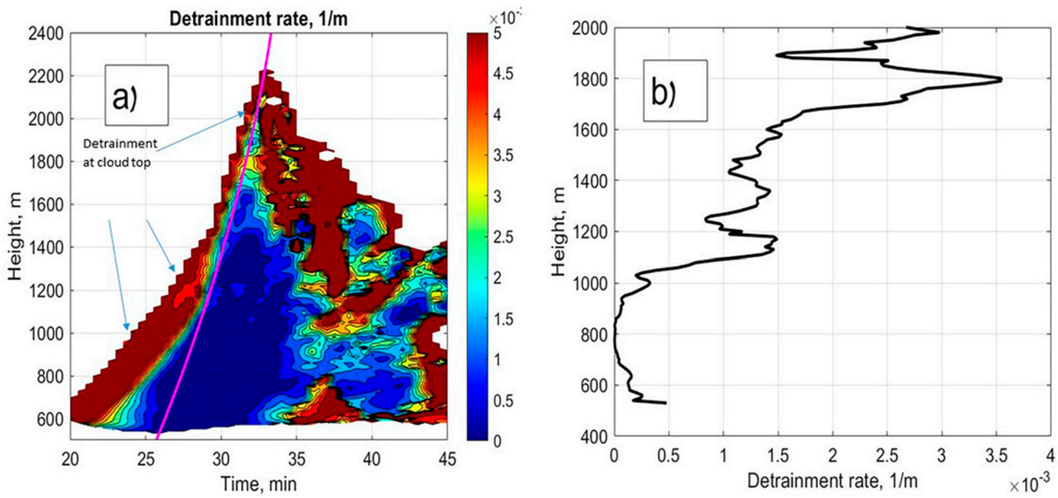

FIG. 22. (a) Height–time field of detrainment rate, $D(z, t)$. The magenta line shows z–t trajectory of the rising point parcel. (b) Vertical profile of the detrainment rate from head bubble.

The finding that lateral dynamical entrainment has a little effect on the top-hat velocity, as well as on the changes in the top-hat conservative variables $\overline{q}_t$ and $\overline{\theta}_l$, requires an explanation and additional investigation. We believe that it can be explained by presence of a toroidal vortex (often approximated by Hill's vortex) whose existence was stressed in many studies (e.g., Zhao and Austin 2005; Houze 2014; Romps et al. 2015; Sherwood et al. 2013). Below we present some evidence concerning the important role of the toroidal vortex, which is not described by the parcel model equations. As shown in Fig. 5, the cloud top ascends nearly parallel to itself like a front, despite the fact that vertical velocity is maximum in the core and decreases toward the CUZ periphery. This effect can be attributed to air divergence at the upper branch of a toroidal vortex. The point parcel determines the maximum cloud-top height. The divergence from the cloud center leads to evaporation of droplets and determines the cloud width (Fig. 5). Although we did not study the internal structure of CUZ in detail, the existence of strong radial motions at the cloud top, which foster its ascent and are directed from the center outward, can be seen in Fig. 22 showing the height–time field of the detrainment rate $D(z, t)$ and the vertical profile of the detrainment rate along z–t trajectory.

One can see that there is a layer of strong detrainment just above the ascending point parcel (in Fig. 22a, the zone above the magenta curve). Comparison of Fig. 22 to Fig. 13 shows that the detrainment rate near the cloud top is several times larger than the entrainment rate. At the same time, the entrainment exceeds the detrainment rate in the lower part of the cloud. This indicates the presence of vortices in the vertical planes, crossing the CUZ. Therefore, it is likely that the central part of the CUZ plays the role of "elevator" that raises air mass and droplets toward the ascending cloud top where the droplets actively evaporate in the divergent air due to mixing with the dry air increasing RH and determining the cloud width.

Acknowledgments. This project has received funding from the European Research Council (ERC) under the European Union's Horizon 2020 research and innovation program (CloudCT, Grant Agreement 810370). This research was supported by the Israel Science Foundation (Grants 2027/17, 2635/20), the Office of Science (BER), and partially supported by Grants DE-SC008811, DE-SC0014295, and ASR DE-FOA-1638 from the U.S. Department of Energy Atmospheric System Research Program.

APPENDIX A

Calculation of Adiabatic LWC Profile

Balance of liquid water in a slowly rising saturated adiabatic volume is described using the equation (e.g., Pruppacher and Klett 1997; Khain and Pinsky 2018)

$$A_2(z)\frac{dq_{\rm ad}}{dt} = A_1(z)\frac{dz}{dt}, \tag{A1}$$

where $q_{\rm ad}$ is adiabatic liquid water mixing ratio, $A_1(z)$ and $A_2(z)$ are slowly changing coefficients dependent on temperature profile $T(z)$, on water vapor mixing ratio $q_v(z)$, and on other thermodynamic quantities:

$$A_1 = \frac{g}{T}\left(\frac{L_w}{c_p R_v T} - \frac{1}{R_a}\right), \quad A_2 = \frac{1}{\rho_v} + \frac{L_w^2}{R_v c_p T^2}, \tag{A2}$$

where g is the gravity acceleration. The other variables can be found in appendix C.

Equation (A1) can be rewritten as $dq_{\rm ad}/dz = A_1(z)/A_2(z)$ and then integrated as

$$q_{\rm ad}(z) = \int_{z0}^{z}\frac{A_1(z)}{A_2(z)}\,dz, \tag{A3}$$

where z_0 is the liquid condensation level. It should be noted that while calculating the adiabatic profiles, data of unperturbed atmosphere are usually used. We used the profiles of a sounding shown in Fig. 1. The data of these profiles coincide with the model data, taken far from zone of developing cloud.

APPENDIX B

Simple Model for Estimation of the Top-Hat Adiabatic Fraction

We consider a vertical velocity inside CUZ, which changes with height z and decreases with the distance r from the center of CUZ:

$$W(r,z) \approx W_{\max}(z)\left[1-\left(\frac{r}{\overline{R}}\right)^{\beta}\right], \tag{B1}$$

where $\overline{R}=(1/z)\int_0^z R(z)dz \approx \text{const}$ is the mean radius of the CUZ and exponent β being independent of r characterizes the rate of vertical velocity decrease in the radial direction. Although radius $R(z)$ varies with height (Fig. 9b), its change is nonsignificant within the height range of 600–1600 m, so $R(z)$ is considered a constant in the first approximation. In the radial direction, the vertical velocity decreases from its maximum at the center, dependent on the height above the cloud base $W_{\max}(z) = W(0, z)$, down to zero at the CUZ boundary. The height z above the cloud base at time instant t can be calculated as (Fig. 18)

$$z(t)=\int_0^t W_{\max}(z)dt=\int_0^t W(0,z)dt. \tag{B2}$$

Since updraft velocity decreases toward the boundary, the vertical distances $h(r, z)$ traveled by different volumes of the air entrained by the rising head bubble and reaching the same height at time instance t are different, decreasing from the center to the boundary

$$h(r,z)=\int_0^t W(r,z)dt=\left[1-\left(\frac{r}{\overline{R}}\right)^{\beta}\right]\int_0^t W_{\max}(z)dt = \left[1-\left(\frac{r}{\overline{R}}\right)^{\beta}\right]z(t). \tag{B3}$$

The height z_0 from which the air volumes start ascending (Fig. 18) is calculated as

$$z_0(r,z)=z(t)-h(r,z)=\left(\frac{r}{\overline{R}}\right)^{\beta}z(t). \tag{B4}$$

In the course of updraft of saturated air elements, the water vapor condenses, and the liquid water is accumulated inside the CUZ according to the equation of condensational growth (see Pruppacher and Klett 1997; or Khain and Pinsky 2018)

$$A_1\frac{dz}{dt}=A_2\frac{dq_l}{dt}, \tag{B5}$$

where q_l is the liquid water mixing ratio (LWC), while A_1 and A_2 are coefficients (see appendixes A and C). Equation (B5) describes the adiabatic profile of liquid water mixing ratio, when supersaturation in a rising head bubble is equal to zero. Equation (B5) can be rewritten as $dq_l(r,z)/dz = A_1(z)/A_2(z)$, which after integration leads to the equation of LWC:

$$q_l(r,z)=\int_{z_0(r)}^{z}\frac{A_1(z)}{A_2(z)}dz=\int_{(r/\overline{R})^{\beta}z}^{z}\frac{A_1(z)}{A_2(z)}dz. \tag{B6}$$

Since coefficients $A_1(z)$ and $A_2(z)$ change with height only slightly, one can calculate an approximate value of $q_l(r, z)$ by integrating Eq. (B6) analytically:

$$q_l(r,z)=\int_{z_0(r)}^{z}\frac{A_1(z)}{A_2(z)}dz=\frac{A_1}{A_2}\left[1-\left(\frac{r}{\overline{R}}\right)^{\beta}\right]z. \tag{B7}$$

The top-hat value of the liquid water mixing ratio $\overline{q}_l(z)$ can be calculated under the assumption of axisymmetry of CUZ:

$$\overline{q}_l(z)=\frac{1}{\pi\overline{R}^2}\int_0^{\overline{R}}\int_0^{2\pi} rq(r,z)d\alpha\, dr=\frac{2A_1z}{\overline{R}^2A_2}\int_0^{\overline{R}} r\left[1-\left(\frac{r}{\overline{R}}\right)^{\beta}\right]dr = \frac{2A_1z}{\overline{R}^2A_2}\frac{\overline{R}^2\beta}{2(2+\beta)}=\frac{A_1z}{A_2}\frac{\beta}{(2+\beta)},$$

so we obtain

$$\overline{q}_l(z)=\frac{A_1z}{A_2}\frac{\beta}{(2+\beta)}. \tag{B8}$$

Since $q_{\text{ad}}(z) = A_1z/A_2$, the top-hat value of the adiabatic fraction depends solely on the exponent value β:

$$\overline{\text{AF}}(z)\approx\frac{\beta}{(2+\beta)}. \tag{B9}$$

APPENDIX C

List of Symbols

Table C1 provides a list of symbols that appear in the paper.

TABLE C1. List of symbols. Note that nd indicates nondimensional values.

Symbol	Description	Units
A_1	$\frac{g}{R_a T}\left(\frac{L_w R_a}{c_p R_v T} - 1\right)$, coefficient	m^{-1}
A_2	$\frac{1}{q_v} + \frac{L_w^2}{c_p R_v T^2}$, coefficient	nd
$\overline{\mathrm{AF}}$	Top-hat adiabatic fraction	nd
B	Buoyancy acceleration	$\mathrm{m\ s}^{-2}$
$\overline{B}$	Top-hat buoyancy acceleration	$\mathrm{m\ s}^{-2}$
c_1, c_2	Coefficients in the motion equation	nd
c_p	Specific heat capacity of moist air at constant pressure	$\mathrm{J\ kg}^{-1}\ \mathrm{K}^{-1}$
D	Entrainment rate	m^{-1}
E	Detrainment rate	m^{-1}
g	Gravitational acceleration	$\mathrm{m}^2\ \mathrm{s}^{-1}$
L_w	Latent heat for liquid water	$\mathrm{J\ kg}^{-1}$
q_l	Liquid-water mixing ratio	$\mathrm{kg\ kg}^{-1}$
q_v	Water vapor mixing ratio	$\mathrm{kg\ kg}^{-1}$
q_{v0}	Reference water vapor mixing ratio	$\mathrm{kg\ kg}^{-1}$
q_{ad}	Adiabatic liquid-water mixing ratio	$\mathrm{kg\ kg}^{-1}$
q_t	Total liquid-water mixing ratio	$\mathrm{kg\ kg}^{-1}$
$\tilde{q}_t$	Total water mixing ratio at the boundary of cloud updraft zone	$\mathrm{kg\ kg}^{-1}$
$\overline{q}_t$	Top-hat total water mixing ratio	$\mathrm{kg\ kg}^{-1}$
R	Radius of cloud updraft zone	m
R_a	Specific gas constant of moist air	$\mathrm{J\ kg}^{-1}\ \mathrm{K}^{-1}$
R_v	Specific gas constant of water vapor	$\mathrm{J\ kg}^{-1}\ \mathrm{K}^{-1}$
r	Radial distance	m
S	Horizontal area of cloud updraft zone	m^2
T	Temperature	K
T_0	Reference temperature	K
t	Time	s
V_R	Radial convective velocity	$\mathrm{m\ s}^{-1}$
W	Convective vertical velocity	$\mathrm{m\ s}^{-1}$
$W_{\max}$	Maximum convective vertical velocity	$\mathrm{m\ s}^{-1}$
$\overline{W}$	Top-hat convective vertical velocity	$\mathrm{m\ s}^{-1}$
w'	Turbulent vertical velocity	$\mathrm{m\ s}^{-1}$
$x\ y$	Horizontal coordinates	m
z	Height above cloud base	m
β	Exponent	nd
γ	Virtual mass coefficient	nd
γ_a	Dry adiabatic gradient	$\mathrm{K\ m}^{-1}$
θ_l	Liquid-water potential temperature	K
$\tilde{\theta}_l$	Liquid-water potential temperature at the boundary of cloud updraft zone	K
$\overline{\theta}_l$	Top-hat liquid-water potential temperature	K
ρ_a	Air density	$\mathrm{kg\ m}^{-3}$
ρ_w	Density of liquid water	$\mathrm{kg\ m}^{-3}$
Φ_z	Flux of vertical velocity	$\mathrm{m}^3\ \mathrm{s}^{-1}$

REFERENCES

Abma, D., T. Heus, and J. P. Mellado, 2013: Direct numerical simulation of evaporative cooling at the lateral boundary of shallow cumulus clouds. *J. Atmos. Sci.*, **70**, 2088–2102, https://doi.org/10.1175/JAS-D-12-0230.1.

Arakawa, A., and W. H. Schubert, 1974: Interaction of a cumulus cloud ensemble with the large-scale environment, part I. *J. Atmos. Sci.*, **31**, 674–701, https://doi.org/10.1175/1520-0469(1974)031<0674:IOACCE>2.0.CO;2.

Blyth, A. M., W. A. Cooper, and J. B. Jensen, 1988: A study of the source of entrained air in Montana cumuli. *J. Atmos. Sci.*, **45**, 3944–3964, https://doi.org/10.1175/1520-0469(1988)045<3944:ASOTSO>2.0.CO;2.

——, S. G. Lasher-Trapp, and W. A. Cooper, 2005: A study of thermals in cumulus clouds. *Quart. J. Roy. Meteor. Soc.*, **131**, 1171–1190, https://doi.org/10.1256/qj.03.180.

Daubechies, I., 1992: *Ten Lectures on Wavelets*. SIAM, 357 pp.

de Roode, S. R., A. P. Siebesma, J. Harm, J. Jonker, and Y. De Voogd, 2012: Parameterization of the vertical velocity equation for shallow cumulus clouds. *Mon. Wea. Rev.*, **140**, 2424–2436, https://doi.org/10.1175/MWR-D-11-00277.1.

de Rooy, W. C., and A. P. Siebesma, 2010: Analytical expressions for entrainment and detrainment in cumulus convection. *Quart. J. Roy. Meteor. Soc.*, **136**, 1216–1227, https://doi.org/10.1002/qj.640.

——, and Coauthors, 2013: Entrainment and detrainment in cumulus convection: An overview. *Quart. J. Roy. Meteor. Soc.*, **139**, 1–19, https://doi.org/10.1002/qj.1959.

Eytan, E., I. Koren, O. Altaratz, M. Pinsky, and A. Khain, 2021: Revisiting adiabatic fraction estimations in cumulus clouds: High-resolution simulations with a passive tracer. *Atmos. Chem. Phys.*, **21**, 16, 203–16 217, https://doi.org/10.5194/acp-21-16203-2021.

——, A. Khain, M. Pinsky, O. Altaratz, J. Shpund, and I. Koren, 2022: Shallow cumulus properties as captured by adiabatic fraction in high-resolution LES simulations. *J. Atmos. Sci.*, **79**, 409–428, https://doi.org/10.1175/JAS-D-21-0201.1.

Fan, J., S. Ghan, M. Ovchinnikov, X. Liu, P. J. Rasch, and A. Korolev, 2011: Representation of Arctic mixed-phase clouds and the Wegener-Bergeron-Findeisen process in climate models: Perspectives from a cloud-resolving study. *J. Geophys. Res.*, **116**, D00T07, https://doi.org/10.1029/2010JD015375.

Gerber, H., 2000: Structure of small cumulus clouds. *Proc. 13th Int. Conf. on Clouds and Precipitation*, Reno, NV, International Commission on Clouds and Precipitation, 105–108.

——, G. M. Frick, J. B. Jensen, and J. G. Hudson, 2008: Entrainment, mixing, and microphysics in trade-wind cumulus. *J. Meteor. Soc. Japan*, **86A**, 87–106, https://doi.org/10.2151/jmsj.86A.87.

Heiblum, R. H., and Coauthors, 2016: Characterization of cumulus cloud fields using trajectories in the center of gravity versus water mass phase space: 2. Aerosol effects on warm convective clouds. *J. Geophys. Res. Atmos.*, **121**, 6356–6373, https://doi.org/10.1002/2015JD024193.

Heus, T., and H. J. J. Jonker, 2008: Subsiding shells around shallow cumulus clouds. *J. Atmos. Sci.*, **65**, 1003–1018, https://doi.org/10.1175/2007JAS2322.1.

——, C. F. Pols, H. J. J. Jonker, H. E. A. Van den Akker, and D. H. Lenschow, 2009: Observational validation of the compensating mass flux through the shell around cumulus clouds. *Quart. J. Roy. Meteor. Soc.*, **135**, 101–112, https://doi.org/10.1002/qj.358.

Houze, R. A., Jr., 2014: *Cloud Dynamics.* 2nd ed. International Geophysics Series, Vol. 104, Academic Press, 432 pp.

Jensen, J. B., P. H. Austin, M. B. Baker, and A. M. Bluth, 1985: Turbulent mixing, spectral evolution and dynamics in a warm cumulus cloud. *J. Atmos. Sci.*, **42**, 173–192, https://doi.org/10.1175/1520-0469(1985)042<0173:TMSEAD>2.0.CO;2.

Katzwinkel, J., H. Siebert, T. Heus, and R. A. Shaw, 2014: Measurements of turbulent mixing and subsiding shells in trade wind cumuli. *J. Atmos. Sci.*, **71**, 2810–2822, https://doi.org/10.1175/JAS-D-13-0222.1.

Khain, A. P., and M. Pinsky, 2018: *Physical Processes in Clouds and Cloud Modeling.* Cambridge University Press, 642 pp.

——, A. Pokrovsky, M. Pinsky, A. Seifert, and V. Philips, 2004: Simulation of effects of atmospheric aerosols on deep turbulent convective clouds by using a spectral microphysics mixed-phase cumulus cloud model. Part I: Model description and possible applications. *J. Atmos. Sci.*, **61**, 2963–2982, https://doi.org/10.1175/JAS-3350.1.

Khain, P., and Coauthors, 2019: Parameterization of vertical profiles of governing microphysical parameters of shallow cumulus cloud ensembles using LES with bin microphysics. *J. Atmos. Sci.*, **76**, 533–560, https://doi.org/10.1175/JAS-D-18-0046.1.

Khairoutdinov, M., and Y. Kogan, 2000: A new cloud physics parameterization in a large-eddy simulation model of marine stratocumulus. *J. Atmos. Sci.*, **128**, 229–243, https://doi.org/10.1175/1520-0493(2000)128<0229:ANCPPI>2.0.CO;2.

——, and D. A. Randall, 2003: Cloud resolving modeling of the ARM summer 1997 IOP: Model formulation, results, uncertainties, and sensitivities. *J. Atmos. Sci.*, **60**, 607–625, https://doi.org/10.1175/1520-0469(2003)060<0607:CRMOTA>2.0.CO;2.

Konwar, M., T. Prabhakaran, A. Khain, and M. Pinsky, 2021: Cloud microphysical structure analysis based on high-resolution in situ measurements. *J. Atmos. Sci.*, **78**, 2265–2285, https://doi.org/10.1175/JAS-D-20-0229.1.

Levine, J., 1959: Spherical vortex theory of bubble-like motion in cumulus clouds. *J. Meteor.*, **16**, 653–662, https://doi.org/10.1175/1520-0469(1959)016<0653:SVTOBL>2.0.CO;2.

McCarthy, J., 1974: Field verification of the relationship between entrainment rate and cumulus cloud diameter. *J. Atmos. Sci.*, **31**, 1028–1039, https://doi.org/10.1175/1520-0469(1974)031<1028:FVOTRB>2.0.CO;2.

Nair, V., T. Heus, and V. Reeuwijk, 2020: Dynamics of subsiding shells in actively growing clouds with vertical updrafts. *J. Atmos. Sci.*, **77**, 1353–1369, https://doi.org/10.1175/JAS-D-19-0018.1.

Norgren, M. S., J. D. Small, H. H. Jonsson, and P. Y. Chuang, 2016: Observational estimates of detrainment and entrainment in non-precipitating shallow cumulus. *Atmos. Chem. Phys.*, **16**, 21–33, https://doi.org/10.5194/acp-16-21-2016.

Ovchinnikov, M. A., and Coauthors, 2014: Intercomparison of large-eddy simulations of Arctic mixed-phase clouds: Importance of ice size distribution assumptions. *J. Adv. Model. Earth Syst.*, **6**, 223–248, https://doi.org/10.1002/2013MS000282.

Pinsky, M., E. Eytan, I. Koren, O. Altaratz, and A. Khain, 2021: Convective and turbulent motions in nonprecipitating Cu. Part I: Method of separation of convective and turbulent motions. *J. Atmos. Sci.*, **78**, 2307–2321, https://doi.org/10.1175/JAS-D-20-0127.1.

Plant, R. S., and J.-I. Yano, 2015: *Theoretical Background and Formulation*. Vol. 1, *Parameterization of Atmospheric Convection*, Imperial College Press, 515 pp.

Pruppacher, H. R., and J. D. Klett, 1997: *Microphysics of Clouds and Precipitation.* 2nd ed. Oxford University Press, 914 pp.

Romps, D. M., , and A. B. Charn, 2015: Sticky thermals: Evidence for a dominant balance between buoyancy and drag in cloud updrafts *J. Atmos. Sci.*, **72**, 2890–2901, https://doi.org/10.1175/JAS-D-15-0042.1.

Scorer, R. S., and F. H. Ludlam, 1953: Bubble theory of penetrative convection. *Quart. J. Roy. Meteor. Soc.*, **79**, 94–103, https://doi.org/10.1002/qj.49707933908.

Sherwood, S. C., D. Hernández–Deckers, M. Colin, and F. Robinson, 2013: Slippery thermals and the cumulus entrainment paradox. *J. Atmos. Sci.*, **70**, 2426–2442, https://doi.org/10.1175/JAS-D-12-0220.1.

Shusser, M., and M. Gharib, 2000: A model for vortex ring formation in a starting buoyant plume. *J. Fluid Mech.*, **416**, 173–185, https://doi.org/10.1017/S0022112000008727.

Simpson, J., and V. Wiggert, 1969: Models of precipitating cumulus towers. *Mon. Wea. Rev.*, **97**, 471–489, https://doi.org/10.1175/1520-0493(1969)097<0471:MOPCT>2.3.CO;2.

Stommel, H., 1947: Entrainment of air into a cumulus cloud. *J. Meteor.*, **4**, 91–94, https://doi.org/10.1175/1520-0469(1947)004<0091:EOAIAC>2.0.CO;2.

——, 1951: Entrainment of air into a cumulus cloud. *J. Atmos. Sci.*, **8**, 127–129, https://doi.org/10.1175/1520-0469(1951)008<0127:EOAIAC>2.0.CO;2.

Tiedtke, M., 1989: A comprehensive mass flux scheme for cumulus parameterization in large-scale models. *Mon. Wea. Rev.*, **117**, 1779–1800, https://doi.org/10.1175/1520-0493(1989)117<1779:ACMFSF>2.0.CO;2.

Turner, J., 1962: The 'starting plume' in neutral surroundings. *J. Fluid Mech.*, **13**, 356–368, https://doi.org/10.1017/S0022112062000762.

——, 1963: Model experiments relating to thermals with increasing buoyancy. *Quart. J. Roy. Meteor. Soc.*, **89**, 62–74, https://doi.org/10.1002/qj.49708937904.

Wendish, M., and J.-L. Brenguier, 2013: In situ measurements of cloud and precipitation particles. *Airborne Measurements for Environmental Research: Methods and Instruments.* Wiley, 225–301.

Zhao, M., and P. H. Austin, 2005: Life cycle of numerically simulated shallow cumulus clouds. Part II: Mixing dynamics. *J. Atmos. Sci.*, **62**, 1291–1310, https://doi.org/10.1175/JAS3415.1.